

AD \_\_\_\_\_

Award Number: DAMD17-98-1-8511

TITLE: A Novel High Resolution Positron Emission Tomography  
System for Measurement of Bone Metabolism

PRINCIPAL INVESTIGATOR: John A. Correia, Ph.D.

CONTRACTING ORGANIZATION: Massachusetts General Hospital  
Boston, MA 02114

REPORT DATE: September 2003

TYPE OF REPORT: Final

PREPARED FOR: U.S. Army Medical Research and Materiel Command  
Fort Detrick, Maryland 21702-5012

DISTRIBUTION STATEMENT: Approved for Public Release;  
Distribution Unlimited

The views, opinions and/or findings contained in this report are those of the author(s) and should not be construed as an official Department of the Army position, policy or decision unless so designated by other documentation.

20040220 048

**REPORT DOCUMENTATION PAGE**Form Approved  
OMB No. 074-0188

Public reporting burden for this collection of information is estimated to average 1 hour per response, including the time for reviewing instructions, searching existing data sources, gathering and maintaining the data needed, and completing and reviewing this collection of information. Send comments regarding this burden estimate or any other aspect of this collection of information, including suggestions for reducing this burden to Washington Headquarters Services, Directorate for Information Operations and Reports, 1215 Jefferson Davis Highway, Suite 1204, Arlington, VA 22202-4302, and to the Office of Management and Budget, Paperwork Reduction Project (0704-0188), Washington, DC 20503

<b>1. AGENCY USE ONLY</b> (Leave blank)		<b>2. REPORT DATE</b> September 2003	<b>3. REPORT TYPE AND DATES COVERED</b> Final (1 Sep 1998 - 31 Aug 2003)	
<b>4. TITLE AND SUBTITLE</b> A Novel High Resolution Positron Emission Tomography System for Measurement of Bone Metabolism			<b>5. FUNDING NUMBERS</b> DAMD17-98-1-8511	
<b>6. AUTHOR(S)</b> John A. Correia, Ph.D.				
<b>7. PERFORMING ORGANIZATION NAME(S) AND ADDRESS(ES)</b> Massachusetts General Hospital Boston, MA 02114  E-Mail: correia@pet.mgh.harvard.edu			<b>8. PERFORMING ORGANIZATION REPORT NUMBER</b>	
<b>9. SPONSORING / MONITORING AGENCY NAME(S) AND ADDRESS(ES)</b> U.S. Army Medical Research and Materiel Command Fort Detrick, Maryland 21702-5012			<b>10. SPONSORING / MONITORING AGENCY REPORT NUMBER</b>	
<b>11. SUPPLEMENTARY NOTES</b>  Original contains color plates: ALL DTIC reproductions will be in black and white				
<b>12a. DISTRIBUTION / AVAILABILITY STATEMENT</b> Approved for Public Release; Distribution Unlimited				<b>12b. DISTRIBUTION CODE</b>
<b>13. ABSTRACT (Maximum 200 Words)</b>  The purpose of the work reported here is to develop high-resolution PET instrumentation for imaging the long bones. To-date a single plane prototype and a single plane second-generation instrumentation have been completed and evaluated. A generalized multi-planar detector element has also been designed and evaluated experimentally and a volumetric instrument has been designed through simulation studies. Radiopharmaceuticals for bone growth rate imaging have been developed for use in a demonstration study of imaging in a monkey osteoporosis model. Preliminary animal studies showing feasibility have been carried out.				
<b>14. SUBJECT TERMS</b>  PET, Instrumentation, Nuclear Medicine, Osteoporosis				<b>15. NUMBER OF PAGES</b>  65
				<b>16. PRICE CODE</b>
<b>17. SECURITY CLASSIFICATION OF REPORT</b> Unclassified	<b>18. SECURITY CLASSIFICATION OF THIS PAGE</b> Unclassified	<b>19. SECURITY CLASSIFICATION OF ABSTRACT</b> Unclassified	<b>20. LIMITATION OF ABSTRACT</b> Unlimited	

## **TABLE OF CONTENTS:**

I. Form 298 .....	page 2
II. Introduction.....	page 4
III. Report Body.....	page 4
A. Background.....	page 4
B. Preliminary and Prototype Design Studies.....	page 5
1. Simulation Studies .....	page 5
2. Design of Blocks and Electronics.....	page 9
3. Design of Data Processing Scheme.....	page 10
4. Evaluation of the Prototype Instrument.....	page 12
C. Second-Generation Design : .....	page 16
1. Introduction.....	page 16
2. Final Detector-Block Design.....	page 17
3. Data Acquisition and Software Development.....	page 18
4. Performance Measurements on Final Instrument.....	page 19
D. Animal Studies.....	page 21
D. Radioabeling Studies.....	page 23
1. Labeling with Iodine.....	page 23
2. 18-F Exchange Labeling.....	page 24
3. <sup>11</sup> C Tetracycline Labeling.....	page 25
F. Detector Block Studies for Volumetric Instrument:.....	page 26
IV. Key Research Accomplishments .....	page 29
V. Reportable Outcomes.....	page 29
VI. Conclusions .....	page 29
VII. Personnel Receiving Support.....	page 30
VIII. Appendix - Publications .....	page 31

## **II. - INTRODUCTION:**

The overall purposes of this project are:

1. To design and develop a PET instrument and methodology for high resolution PET imaging of the long bones.
2. Develop a radiopharmaceutical to image bone growth rate.
3. Demonstrate the use of this device in a limited experimental protocol to assess estrogen therapy for in a monkey model.

The first aim has been met and exceeded. We have designed and constructed two instruments having resolution of approximately 1mm. The first was an experimental prototype in which the design concepts were explored and tested. The second was a modified version of the first into which improvements were introduced based on our experience with the prototype. Also, simulation and experimental studies to extend the design to a volumetric (multi-planar) instrument have been successfully carried out.

The second aim has been met by the design of labeling methods for  $^{124}\text{I}$ -Tetracycline and  $^{11}\text{C}$ -tetracycline. Methods for labeling  $^{18}\text{F}$ -Tetracycline were also pursued with limited success.

The third aim was not met due to the limited availability of  $^{124}\text{I}$  for labeling and the unsuitability of the  $^{11}\text{C}$  compound due to its short half-life.

However, a limited series of monkey studies using  $^{18}\text{F}$ -fluoride ion were carried out to demonstrate feasibility and an extensive series of several hundred rat and mouse studies were carried out in support of a related DOD program using the instrumentation developed.

## **III. - REPORT BODY:**

### **A. - Background:**

PET (positron emission tomography) imaging is a nuclear medicine technique for measuring quantitative regional physiology and biochemistry in intact animals and humans. The penetrating radiation resulting from positron decay is in the form of two 511 keV photons which are time-correlated and leave the site of the decay in approximately opposite directions. PET imaging devices are designed to detect these photon-pairs as coincidence events. Detection of the photon pairs is the basis for the ability to fully correct for physical effects such as source self-absorption and photon scatter. Application of these corrections makes possible quantitative measurement radioactivity distributions. Large-scale PET devices (for human and large animal imaging) are highly evolved and commercially available. The frontier in PET imaging instrumentation lies in

developing high resolution, small-scale devices for imaging small animals or, in the case of this work, extremities. The advent of new radiation-detector materials, particularly new scintillators such as Lutetium Orthosilicate (LSO) has made it possible to build such a small-scale device in practice.

The first year's work emphasized the design of an instrument for imaging primate extremities, mice and possibly human extremities in the future. The approach was to carry out simulation studies of physical and instrument factors as well as design and feasibility experiments in order to optimize the system design. Then a complete prototype instrument was constructed as an experimental platform for development of detector module designs, electronics, software for coincidence identification, and physical imaging studies. As a result a final configuration for the device proposed in this was established and construction begun.

The second year's work consisted mainly of construction of the second-generation device and associated software and its initial physical evaluation. As an ancillary project related to the main aim of developing a device for bone imaging, the design of a detector module for a volumetric (multi-planar) detector was begun, a prototype detector module constructed and physical evaluation experiments undertaken.

During the third we completed construction of the second, final single-plane instrument, explored methods of improving its performance, developed a design for a generalized volumetric version of the instrument and pursued the radiochemical synthesis of  $^{11}\text{C}$  and  $^{18}\text{F}$  tetracycline. The single plane instrument was also used in a number of small-animal studies funded under a related DOD project at our institution (DAMD-17-99-1-9555, Dr. A. Brownell, principal investigator).

In the fourth and fifth (extension) year we continued the refinement of the existing single plane instrument, pursued the design of a volumetric extension to this instrument, continued development studies to label tetracyclines and carried out preliminary monkey studies. The full monkey experiment as proposed was not completed due to the lack of availability of  $^{124}\text{I}$  for labeling tetracycline. The shorter half-life  $^{11}\text{C}$  compound that was developed proved not to have a long enough half-life for the imaging studies and an  $^{18}\text{F}$  compound is still under development.

The details of the development studies outlined above are presented in previous reports and in the appended publications and will be outlined below.

## B. Preliminary and Prototype-Design Studies.

### 1. - Simulation Studies:

The parameters of importance in designing a small-scale PET instrument include detector diameter, detector-element dimensions, shielding and coincidence-to-single-event ratio. These parameters determine the system sensitivity, resolution and count-rate capability.

The performance of small-scale single-plane PET geometries was studied using both Monte Carlo simulation and computation. The purpose of these studies was to characterize the expected performance of small diameter instruments. Effects taken into account in the simulations included detailed properties of the radiation emission and interaction, detector array geometry, shielding geometry and detector material properties. The Monte Carlo studies were carried out in detail for the 12cm diameter prototype and for the 15cm diameter instrument, which was initially proposed. Also, several other diameters were studied with a more limited subset of simulations. Studies were done at axial detector openings ( $z$ ) of 0.5 and 0.25cm. This parameter affects both the sensitivity and the  $z$  axis resolution. Lead (Pb) shielding with an imaging aperture of half the detector diameter was assumed. For each geometry, the diameter of a cylindrical source of radioactivity and the detector energy thresholds were varied. Detailed results of these studies have been previously reported. Sample results for the 15cm diameter device are presented in figures 1a-1d. Figures 1a and 1b show the single event and coincidence event scatter fractions for 20 million coincidence events emitted from cylindrical sources of various diameters. The fraction of scattered coincidences is typically very low ( $< 3\%$  in the worst case of a 5cm-diameter source) and agrees well with the experimental measurements. Figure 1c shows the single event-to-coincidence-event ratio as a function of source diameter, again for a total of 20 million events. Figure 1d, which incorporates the detector efficiency data of figure 2, shows the sensitivity of the instrument as a function of source diameter for 7mm deep LSO crystals. The data in figures 1a-1d are for a 125 keV energy threshold.

Conclusions from these studies are as follows: (1) results for the 12cm diameter prototype agree well experimental measurements from the prototype (2) A larger 15cm diameter device will perform acceptably for bone imaging (3) The geometries studied yield an acceptably low scattered coincidence fraction (4) The coincidence-event to single-event ratios, which affect system dead time, are acceptably low for the designs studied.

Monte Carlo simulations of detection efficiency for LSO and other materials and detector penetration effects for 1 and 1.2mm wide LSO detectors were also carried out to determine optimum crystal length. Figure 3 shows the results for LSO at three energy threshold levels. The prototype device was constructed using 5mm deep crystals and a 125 keV energy threshold to minimize multiple-interaction events within the detectors. This results in a single-event detector efficiency of approximately 25% at 125 keV threshold and a coincidence sensitivity (square of single detector efficiency) of approximately 6.3%. If the depth of the detectors were extended to 7mm the coincidence efficiency would be increased to approximately 12%.

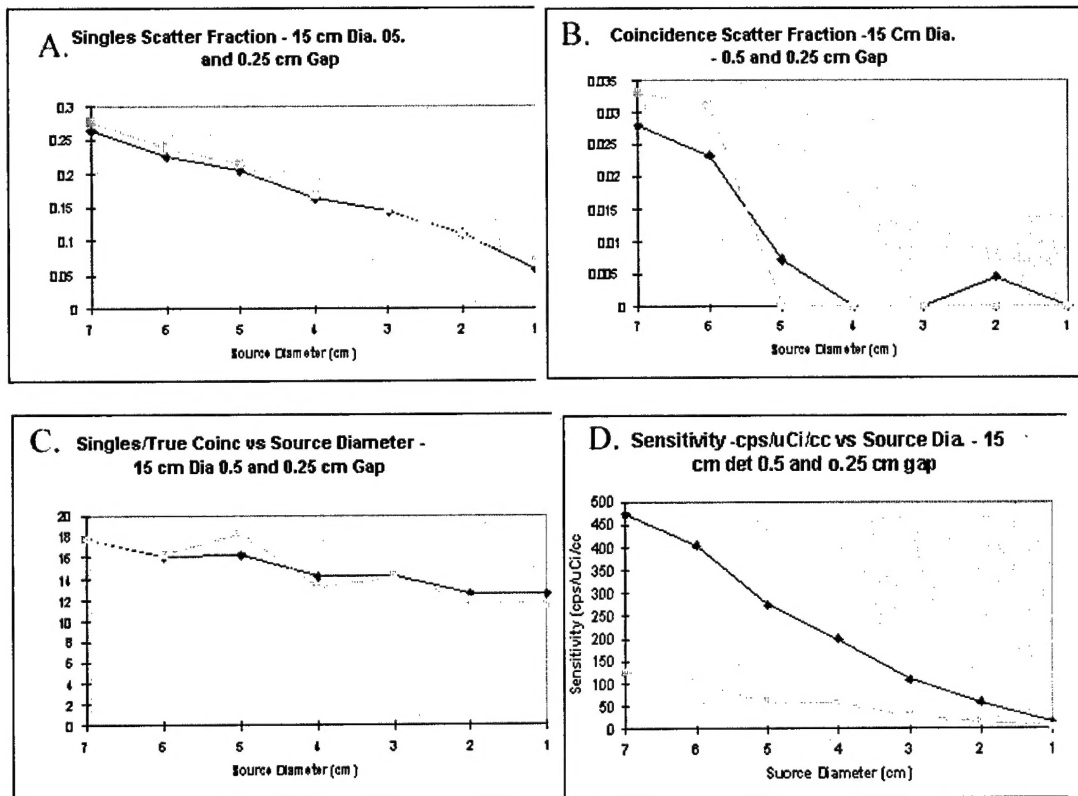


**Figure 1a:** Monte Carlo simulation of fraction of single events scattered for a 15cm diameter detector ring as a function of the diameter of a 10cm long cylindrical source and an 8cm imaging aperture. Vertical (z) detector opening of 0.5 and 0.25cm. 20 Million events simulated.

**Figure 1b:** Monte Carlo simulation of fraction of coincidence events scattered for a 15cm diameter detector ring as a function of the diameter of a 10cm long cylindrical source and an 8cm imaging aperture. Vertical (z) detector opening of 0.5 cm. 20 Million events simulated.

**Figure 1c:** Monte Carlo simulation of single/coincidence ratio for a 15cm diameter detector ring as a function of the diameter of a 10cm long cylindrical source and an 8cm imaging aperture. Vertical (z) detector opening of 0.5 and 0.25cm. 20 Million events simulated.

**Figure 1d:** Monte Carlo simulation raw system sensitivity including detector efficiency for a 15cm diameter detector ring as a function of the diameter of a 10cm long cylindrical source and an 8cm imaging aperture. Vertical (z) detector opening of 0.5 and 0.25cm. 20 Million events simulated.

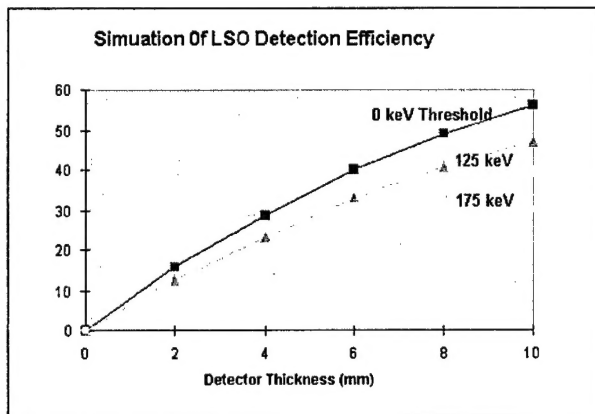


Figure 2: Monte Carlo simulation of 511 keV photon efficiency for LSO as a function of depth at several energy thresholds.

were calculated for a series of detector diameters and crystal lengths. An example of the results is shown in figure 3 which presents a calculation of this penetration effect for 5mm thick detectors in the 12cm diameter detector ring. The experimental resolution measurements shown in a later section support the conclusion that this is a tractable effect, especially if objects imaged are limited to the central half of the field, and therefore correction for crystal penetration effect is not necessary. Since it is desirable that the final design have a larger diameter than the prototype to accommodate bigger objects, the same penetration effect was studied for a 15cm ring and 7mm deep detectors. A 7mm deep detector would result in a 12% coincidence efficiency (96% increase over a 5mm detector) while the resulting loss in overall instrument efficiency due to an increase in diameter would be only 25%. The penetration curves for a 15-cm diameter and 7mm detectors are the same shape as those of figure 4 with the y-axis increased to increased detector depth. It may be concluded that, if imaging is limited to the central half of the field no correction for penetration effects in a 15cm design is necessary.

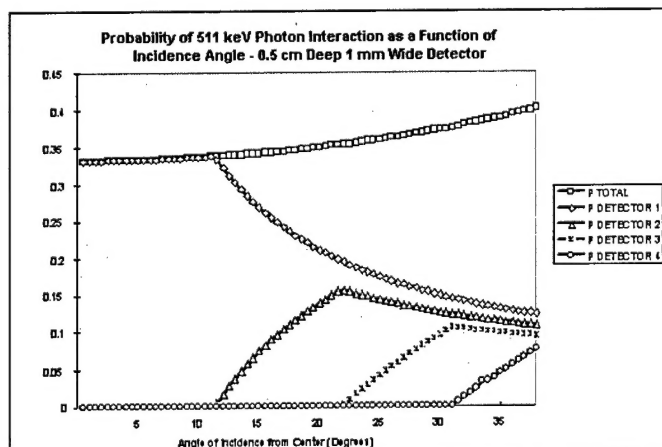


Figure 3: Detector penetration as a function of photon incidence angle for 1x4.5x5mm LSO detector array. The top curve shows total probability of interaction. The four lower curves represent, respectively, the primary detector and each of the three adjacent detectors along the photon's geometric path. The central third of the detector field has a limiting incidence angle of 19 degrees. The same dataset for a 15 centimeter ring and 7mm deep detectors looks essentially the same with the y axis scaled up by approximately a factor of 1.5.

A major limitation to achieving high resolution is the penetration of photons into detector elements adjacent to the primary element when such photons are incident at angles other than 90 degrees. If longer detectors are used to increase efficiency the effect of this penetration becomes larger for a given detector-ring diameter. This is a major reason for choosing short detectors. Penetration effects

Based on the properties of the prototype and information from the literature concerning the behavior of fluorescent (non-radioactive) tetracycline compounds, calculations were carried out to determine if a reasonable PET signal would be obtained from a labeled

tetracycline. This is an important issue since the thickness of the growth bands in primate long bones is quite small, on the order of 100 $\mu$ . The calculations use properties of fluorescent tetracycline kinetics from the literature and tissue radioactivity data from PET primate experiments at our laboratory. From the results, shown in figures 4a and 4b, it may be concluded that the measurement of bone growth rings in monkey long bones is feasible with reasonable injected doses of radioactivity (20-75 mCi). Although the signal is small, the high resolution of the imaging device allows separation of the inner and outer surfaces of the long bones and changes in growth rate with time on the order of 10% is easily detectable in monkeys.

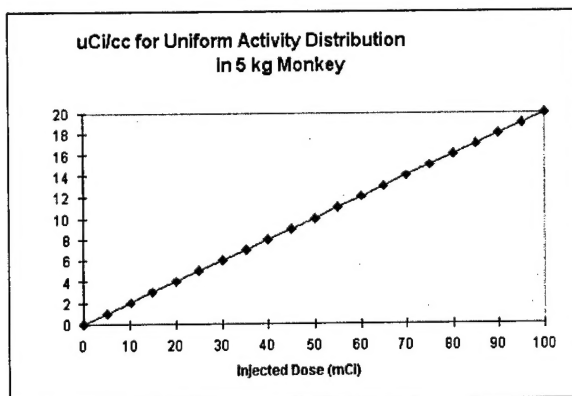


Figure 4a: Tissue radioactivity concentration in a 5kg monkey vs injected dose. Assumption of uniform radioactivity distribution is made.

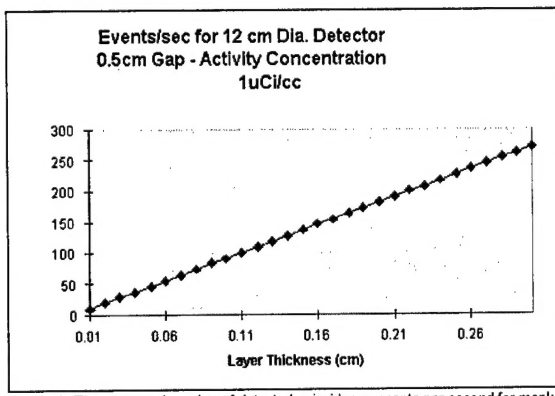


Figure 4b: The computed number of detected coincidence events per second for monkey long bone layers of various thicknesses having a concentration of 1 uCi/cc.

## 2. Design of Blocks and Electronics:

A schematic diagram of the prototype system is shown in figure 6. The detector array consists of a single ring of 360 1x4.5x5mm LSO crystals organized into blocks of 12 crystals each, viewed by two photomultiplier tubes (PMT's). The diameter of the detector array is 12cm. The preamplifiers, coincidence circuits and digital conversion circuits were implemented using standard logic elements. In the course of setting up the prototype a number of circuit board designs were generated. These included a PMT preamplifier, event processing boards, a coincidence circuit and a board, which transfers coincidence data sets to a computer interface. All of these designs functioned well in the prototype and were therefore used in the final instrument. The preamplifier layout was changed to incorporate modifications made during development.

In the detector block, it is required that some fraction of the scintillation light from any crystal reach each the PMT's viewing that block. This requires that the surfaces of the crystals be treated in different ways depending on their position within the block. A number of different surface combinations were studied both by computer simulation of the light optics and by construction of prototype crystal blocks. Preliminary designs for both a 12 crystal block with 1mm resolution and a 10 crystal block with 1.2mm resolution were established and test-blocks evaluated. Based on the results of these studies a set of 30 12-crystal blocks

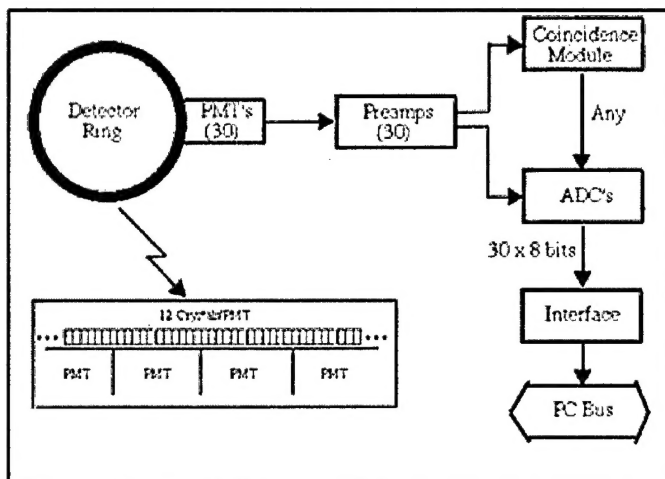


Figure 6: Prototype system diagram showing data acquisition front end electronics.

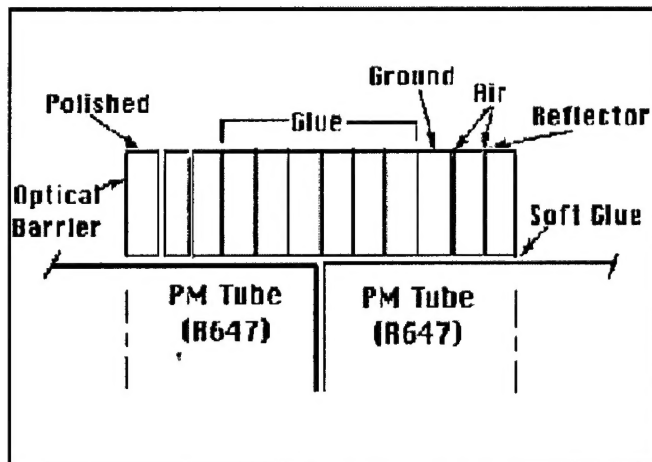


Figure 7: Diagram of LSO 12 crystal block attached to two phot tubes. Various surface preparations for light distribution are shown.

A simple ISA-bus-based data acquisition interface was constructed to acquire test data from the prototype system. Based on the experience gained with this interface, a number of commercially available PCI-Bus-based data acquisition interfaces were evaluated and the one most suited to our situation was chosen.

### 3. Design of Data Processing Scheme:

Each block of twelve crystals is viewed by two adjacent PMT's. Signals from these PMT's, which are proportional to the light reaching each, are used to compute the identity the crystal in which a given event originated. The details this computation are as follows. Once a coincidence event is registered by the hardware and the 30 PMT signals are transferred to the computer. The sum of neighboring pairs of PMT signals is computed. When a sum exceeds both

was constructed in an attempt to achieve 1mm instrument resolution. As will be mentioned below, the prototype ultimately achieved 1.2mm resolution due to limitations in the performance of the blocks. It was therefore decided to construct the final system to a specification of 1.2mm resolution using 1.2mm crystals.

To fabricate the prototype blocks, the eight interior crystal faces were glued together in a jig with an 8° taper in order to point them toward the ring center. The next two on each side were separated from the central crystals and each other by an air gap as illustrated in figure 7. A major technical accomplishment of the project was the development of a method for fabricating the blocks with all crystals pointing toward the instrument's center.

neighboring sums and an energy threshold, a block is identified. When exactly two blocks are identified within a data set the processing proceeds to the identification of the individual crystals within each. The normalized difference ( $R$ ) of photomultiplier signals ( $A$  and  $B$ ) in each block is determined as follows:

$$(1) \quad R = (A - kB) / (A + kB)$$

and if an energy criterion to select only events about the photopeak:

$$(2) \quad E > E_{\text{threshold}} \quad \text{and} \quad E_{\text{lower}} < E < E_{\text{upper}}$$

is met, a particular crystal is identified, otherwise the event is rejected.

A given value of  $R$  is associated with an individual crystal within the block via a lookup table specifying the lower and upper levels of the ratio values for that crystal. A good event is recorded if the boundary conditions are met and the PMT-sum, or total energy, signal is within a window derived from the crystal energy spectra. Boundary and energy lookup tables are specified for each block to account for small variations in crystal properties and alignment among blocks. In addition a third block specific lookup table ( $k$  in equation 1) is used to normalize the  $R$  spectrum to zero at the center of each block. The determination of the lookup tables is an iterative process in which a starting set of boundaries are specified from  $R$  plots with wide energy windows, then a set of narrower energy windows are specified from the energy spectra and the process repeated until an optimum is reached. Figures 8 and 9 show a normalized difference spectrum and crystal energy spectra, respectively, from a typical block. It should be noted that the separation of the end crystals is less complete than those at the center. The above-described algorithm and tuning method have been extensively tested in the prototype.

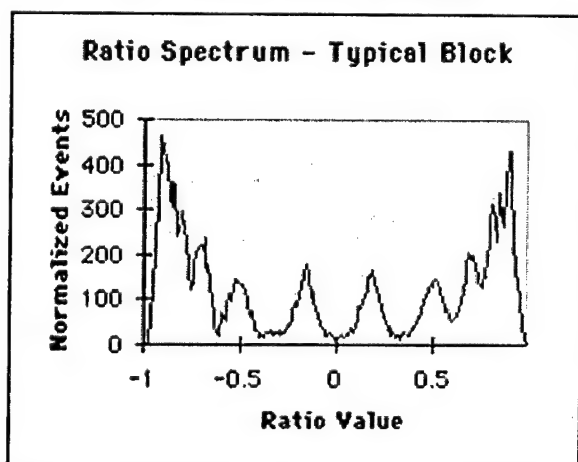


Figure 8: Normalized difference Spectrum from a Typical Block Measured with  $^{68}\text{Ge}$ . Photofraction events. Note that the outer crystals are not fully resolved in this block consisting of twelve 1mm crystals.

Coincidence data are mapped to a sinogram format for storage. The sinogram format is a histogram of events as a function of field radius and angular position. It is a representation that is convenient for image reconstruction and has been used in most earlier PET scanners. The sinogram is subsequently corrected for sensitivity and reconstructed using a standard convolution-back-projection algorithm.

From the studies carried out with the prototype blocks it was concluded that the maximum system resolution of 1mm was not achieved due to several factors including limitations of light collection from the crystals, small

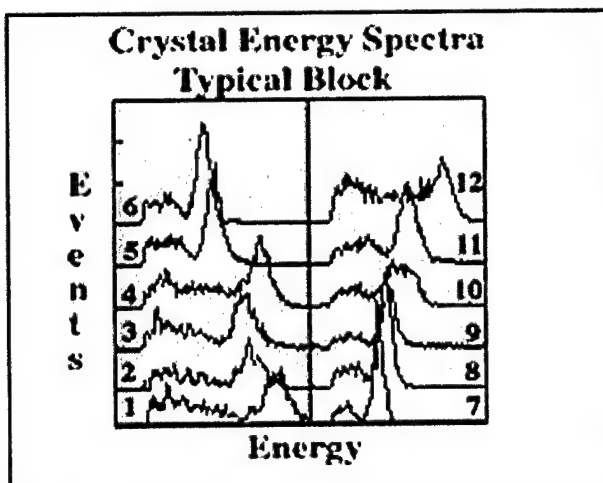


Figure 9: Energy spectra measured from a typical block using a  $^{68}\text{Ge}$  source. Crystal numbers within the block are indicated at the sides.

imprecision in the alignment of crystals within the blocks, relatively poor energy resolution near the center of the blocks, and limitations of the original preamplifier design. Based on these results we redesigned the preamplifier and made the decision that the final instrument would be constructed with 1.2mm crystals yielding a system resolution of 1.2mm with considerably better block performance. All other circuit components designed for the prototype system functioned well and therefore the same designs

were used in the final system.

#### 4. Evaluation of the Prototype Instrument:

A photograph of the prototype is shown in figure 10. Some of the most important parameters to be considered in a PET system are the spatial resolution, sensitivity, countrate capability, field uniformity, and ability to reproduce radioactivity concentrations over a wide dynamic range. Physical measurements of these parameters have been made on the prototype. Examples of the results are presented in figures 11-15 and tables 1 and 2 and are discussed below.

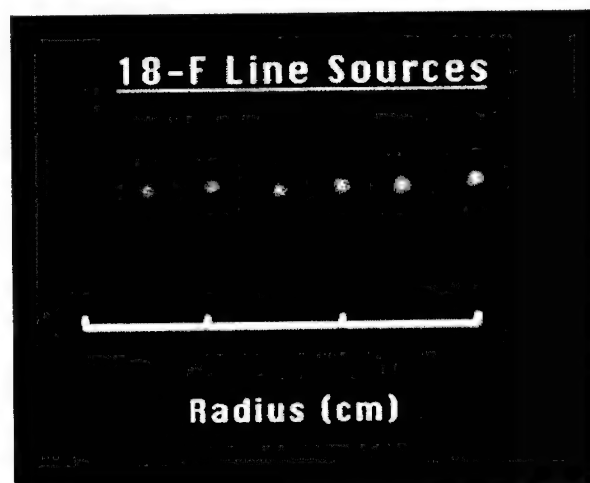
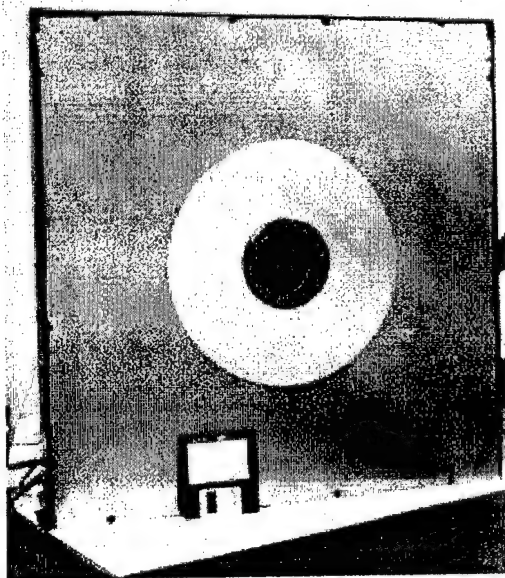


**Figure 10:** Photo of 12 cm diameter prototype 0.4mm With 6 cm imaging aperture. A 3. Inch disk is shown for scale.

**Figure 11:** Reconstructed Image of six  $^{18}\text{F}$  line sources 0.5 cm apart. The scale shown is at 1 cm intervals and center of the image is at the center of the field.

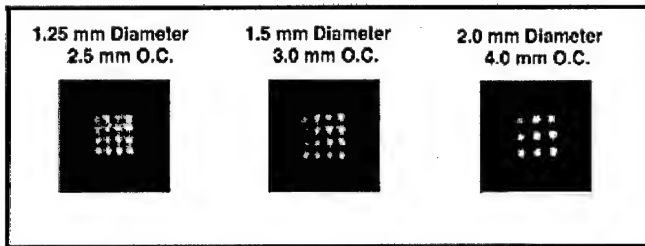


**Figure 12:** Reconstructed images of 1x1x0.75 cm high polystyrene cubes having  $^{18}\text{F}$ -filled wells. The well diameters and separations are indicated.

Figure 11 shows a reconstructed image of 6 "point" sources of  $^{18}\text{F}$  radioactivity which consists of 0.4mm i.d. needles placed perpendicular to the imaging plane spaced radially at 5mm intervals starting at the field center. Table 1 summarizes the resolution measured at each position (resolution is full width at half maximum of a profile through the center of each source). At the center the resolution is 1.25mm and degrades to 1.6mm at 2.5cm radius due to detector penetration effects. However, within a central circle of about 1.75cm radius only minimal degradation is observed. The axial resolution (or effective imaging plane thickness) at the center of the field was measured by moving a point source of  $^{18}\text{F}$  axially through the field in 0.1mm steps. It should be noted that the axial resolution can be reduced by narrowing the gap in the Pb collimators which define the imaging gap at a sacrifice of sensitivity that is inverse to the square of the reduction. Figure 12 shows an alliterative measure of resolution. Images of small squares of plastic, which have arrays of  $^{18}\text{F}$ -filled wells of various diameters and separations, are shown. The smallest set, 1.5mm diameter with 2.5mm separation, are completely resolved.

**Table 1:** Spatial Resolution at Various Field Radii Measured from the 0.4mm Diameter Line Sources of figure 10. Axial Resolution was measured by moving a point source of  $^{18}\text{F}$  through the field in 1-mm steps. Full Width at Half Maximum (FWHM) and Full Width at Tenth Maximum (FWTM) for each source.

RADIUS (cm)	FWHM (mm)	FWTM (mm)
0	1.25	2.45
0.5	1.23	2.50
1.0	1.30	2.60
1.5	1.35	2.60
2.0	1.61	3.0
2.5	1.72	3.0
Axial(Center)	1.8	3.4

The system sensitivity was measured using cylindrical sources of  $^{18}\text{F}$  radioactivity of varying diameter and a point source of  $^{18}\text{F}$  at the center of the field. The sensitivity as measured here represents all coincidence events above a 125 keV threshold. The corresponding computed sensitivities determined from the Monte Carlo simulations agree fairly well with the measurements as shown in table 2.

**Table 2:** Measured sensitivity for cylindrical objects of varying diameter and for a point source at the field center. The measurements include all events above 125 keV. Monte Carlo simulation results are shown for comparison.

Source diameter (cm)	Measured Sensitivity (cps/uCi/cc)	Computed Sensitivity (cps/uCi/cc)
0.5	3	-
2.0	40	52
2.5	69	86
3.5	145	162
4.5	204	230
Point	30 cps/uCi	70 cps/uCi

Figure 13 shows measurements of the system's response to a range of radioactivity concentrations in small objects. A test object consisting of five 2.7mm diameter cylinders containing various concentrations of  $^{18}\text{F}$  radioactivity in a 3.5cm diameter water absorber was imaged. The measurement was then repeated over several ranges of radioactivity and relative radioactivity concentrations in the small cylinders measured from the reconstructed images. Figure 13 shows a plot of PET measured radioactivity concentration versus actual concentration measured by a well counter along with a linear least squares fit to the experimental points.

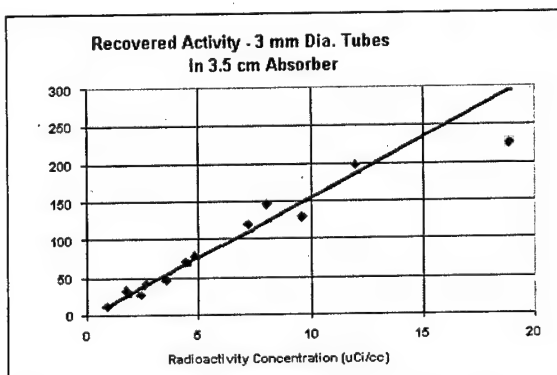


**Figure 13:** Reconstructed radioactivity concentration in 3mm cylinders as Versus known concentration. A linear least squares fit to the data is also shown.

The overall conclusions that may be drawn from the above-described measurements are as follows:

1. The best system resolution is 1.25mm rather than the 1-mm expected based on system design. This may be explained by the relatively poor

identification of the outer crystals in the blocks, the presence of small alignment errors in the crystals and poor energy resolution at the center of the blocks due to poor light collection.

2. The overall sensitivity is in fairly good agreement with simulation results although the measured results are systematically lower.
3. The recovery of radioactivity is linear over a wide range of concentrations from 0.05-18uCi/cc.
4. The central field region is uniform to less than 5%.
5. The system support countrates up to 100,000 coincidences per second with little front-end deadtime. The more practical limit of random coincidences comprising more than half the signal is reached at about 70k total coincidences/sec, well below the rates where deadtime becomes significant.
- 6.

A summary of the performance characteristics of the prototype device is given in table 3.

Table 3: Specifications of 12 cm Diameter Prototype PET Instrument

<b>PARAMETER</b>	<b>VALUE</b>
<b>Number of Planes</b>	1
<b>Detector Array Diameter</b>	12 cm
<b>Number of Crystals/Type</b>	360/LSO
<b>Crystal Dimensions</b>	1 x 4.5 x 5mm
<b>Number of Phototubes/Blocks</b>	30
<b>In-Plane Spatial Resolution</b>	1.2 mm center - 1.6 mm at 2.5cm
<b>Axial Resolution</b>	0.25 – 0.5 mm
<b>Field of View</b>	8 cm
<b>Point Source Sensitivity</b>	30 coincidences/second/uCi
<b>Field Uniformity</b>	< 5% variation in 3.5 cm disk
<b>Randome=Trues</b>	70000 conic./sec

### C. Second-Generation Design for Primate and Human arm Imaging:

#### 1. Introduction:

Based on the simulation, computational and experimental studies carried out a design for the final device to be constructed for bone imaging was generated. The main features of the design are given in Table 4. The main differences from the prototype in addition to a newly designed preamplifier are:

1. Wider LSO crystal elements, 1.2 mm rather than 1, to give better block performance at 1.2mm resolution.
2. 14.5cm detector array diameter.
3. Longer LSO crystal elements to improve sensitivity. 7mm rather than 5mm.
4. More phototube channels, 36 rather than 30 to accommodate the larger diameter.
5. Windows 95/98-based data acquisition interface which consists of a PCI data channel and a FIFO buffer to eliminate interface dead time.
6. Corrections for deadtime, accidental coincidences and scattered photons leading to full quantitation.

In addition, we have designed a moving mechanical arm support, which operates under computer control and is integrated with the data acquisition software.

Table 4: Specifications of 15 cm Diameter PET Instrument

PARAMETER	VALUE
Number of Planes	1
Detector Array Diameter	14.5 cm
Number of Crystals/Type	360/LSO
Crystal Dimensions	1.25 x 5 x 7mm
Number of Phototubes/Blocks	36
In-Plane Spatial Resolution	1.25 mm center - 1.6 mm at 3cm
Axial Resolution	0.25 – 0.5 mm
Field of View	8 cm
Point Source Sensitivity	50 coincidences/second/uCi/cc
Field Uniformity	< 3% variation in 4.5 cm disk
Randome=Trues	60000 conic./sec

## 2. Final Detector-Block Design for Single-Plane Instrument:

The results of the design and experimental studies carried out in the first year of the project indicated that the 1mm resolution at the field center, dictated by sampling was not achieved due to performance limitations of the 12 crystal detector blocks. Further some loss of sensitivity due to this limited performance was observed in the prototype device. It was therefore decided to use slightly wider LSO crystals (1.2 mm) in the final design. Such wide crystals would limit the maximum resolution to the 1.2-mm achieved with the prototype but would improve the performance of the blocks considerably. Further, it was decided to increase the depth of the crystals from 5mm to 7 mm resulting in a factor of 2 improvement in sensitivity from this source alone. Figure 14 shows a schematic diagram of the new detector block. Experimental studies to optimize

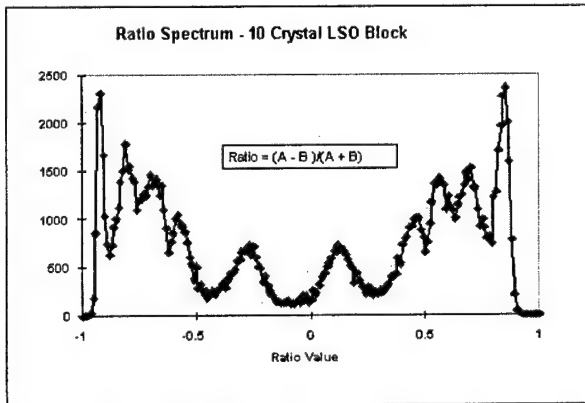


Figure 15: Measured ratio Spectrum for ten-crystal block. The end crystals are more clearly resolved than those in the prototype block. Also, the dynamic range between the center and edge crystals is lower than the corresponding range in the twelve-crystal block indicating better light collection at the block center

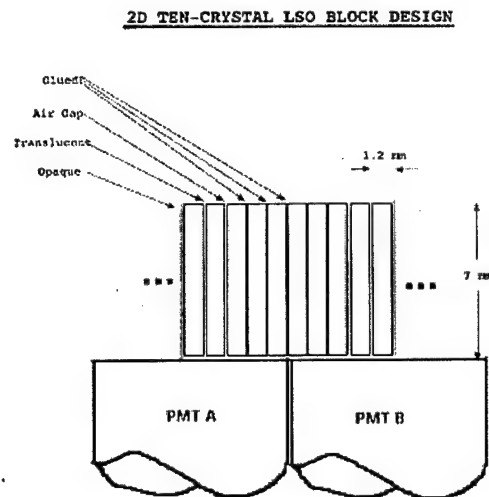


Figure 14: Schematic of ten crystal LSO block showing surface treatments.

the propagation of light within the blocks led to the surface preparations shown in the diagram. Figure 15 shows the ratio spectrum resulting from measurement of 511 keV photons from a uniform source. The ten crystals are identified well.

## 3. - Electronic Design and Board Layouts:

A schematic diagram of the second-generation electronics is shown in

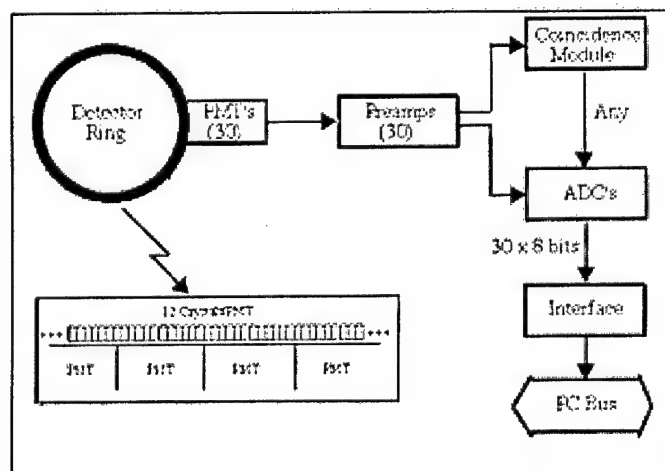


Figure 16 : System diagram showing front end electronics.

figure 16. Part of the goal in designing the instrument was to minimize the need for specialized electronics by making maximal use of software-based processing. Each PMT signal is processed by its preamplifier board to yield a timing pulse and an energy pulse. Leading-edge timing and delay-line shaping are used to identify coincident events. Coincidences are determined among groups of ten PMT signals. Once a coincidence is identified, all 36 PMT signals are digitized by the ADC boards and transferred as a group to the computer interface. Two of the spare ADC channels are used to transfer the total single event rate, which is used to generate a random coincidence correction.

The following circuit boards were laid out using ORCAD software and manufactured by an outside vendor:

1. Preamplifier Boards - 36
2. ADC Boards - 10
3. Coincidence Board - 1
4. Interface Board - 1

#### 4. Data Acquisition and Software Development:

##### a. Data acquisition:

One of the limitations of the prototype instrument was its inability to collect data at high countrates. To overcome this limitation a number of data acquisition hardware and software configurations were studied. In order to take advantage of the large body of development work that had been carried out in the PC-based data acquisition area, it was decided to pursue commercially available acquisition hardware, which uses the PCI Bus interface for the PC. The main requirements for the instrument are acquisition speed, or data rate, ability to interface to the analog electronics and ability to buffer incoming data so that front-end processing can be carried out during acquisition. Test software was written for several commercially available boards as well as for an enhanced version of our in-house developed acquisition board. The best commercial device evaluated, the PCIDIO3240 board manufactured by CyberSystems, was incorporated into the second-generation system.

##### b. Image Manipulation and Display Software:

Two display packages have been set up for the imaging system. The first was written in MATLAB Graphical Interface Language. In the course of investigating display systems we discovered a public domain display program which was originally written at NIH but is now available (free) through a commercial supplier. This fully functional display package, originally written for use with autoradiographic data, has been adapted with minor changes. The features common to both programs include grayscale and color display of both sinograms and reconstructed images: Region-of-interest selection and extraction

of data, profile extraction, image arithmetic and image processing (smoothing, etc).

c. Software Development:

In order to collect, reconstruct and display PET data, a number of software modules are necessary. Our approach was to develop software for the prototype device using C/C++ code in the Windows95/98 operating system. Software modules developed for the prototype system were adapted and modified for use with the new system under Windows95/98. New features added include collection sequence editor, multiple frame collection with optional object motion, an automated sequential file naming routine and new file headers carrying complete information with each sinogram or image file. In addition implementation of corrections, scatter, deadtime, attenuation, uniformity and radioactive decay in the new software package is ongoing. Some of these corrections, uniformity and attenuation in particular, have been implemented in the prototype while the remaining ones are new to the final instrument.

d. Automatic Motion System:

In order to collect sequential images of long bones or small animals, it is necessary to have some method of moving objects reproducibly within the instrument's field-of-view. Ideally, the control of this device should be integrated with the camera control software for both ease of use and centralization of image information (i.e., storage of all image information in an image file header). To accomplish this we have adapted a commercially available motion controller and stepping motor. A software module to control this device and read position has been integrated into the data acquisition program. In the final version of the software, an object's position relative to an initial reference position can be specified and the object moved to that position before the start of each frame; the position being recorded with the frame data. An option for user-specified (non-automated) positioning is also provided.

5. Performance Measurements on Second-Generation Instrument:

The in-plane spatial resolution was measured with small-diameter (0.4mm)  $^{18}\text{F}$ -line sources and the results are given in figure 17. The measured in-plane resolution is 1.25mm FWHM at the center of the field and 1.5mm FWHM at two-cm radius. The FWMTM is also illustrated in figure 17. The measured system sensitivity for both a point source and a 4.5cm cylindrical source are shown in table 5. They are compared to the same quantities for the prototype instrument. A twofold increase in sensitivity results from a combination of increased crystal thickness, improved event identification at the block centers and an increase in detector ring diameter from 12.4 to 14.7cm.

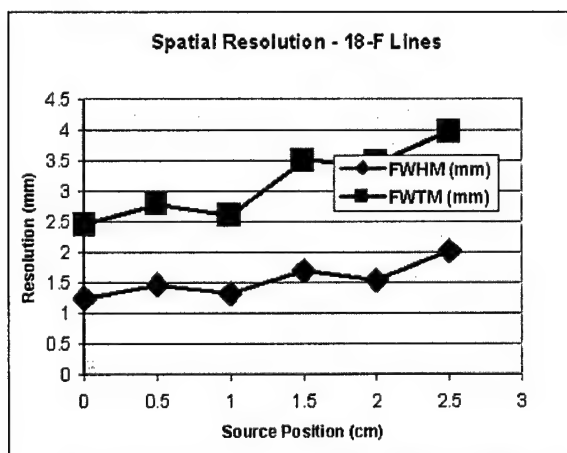


Figure 17: Spatial resolution as a function of field radius measured with 0.42 mm 18-F line sources. Measurements are corrected for source size. FWHM and FWTM shown.

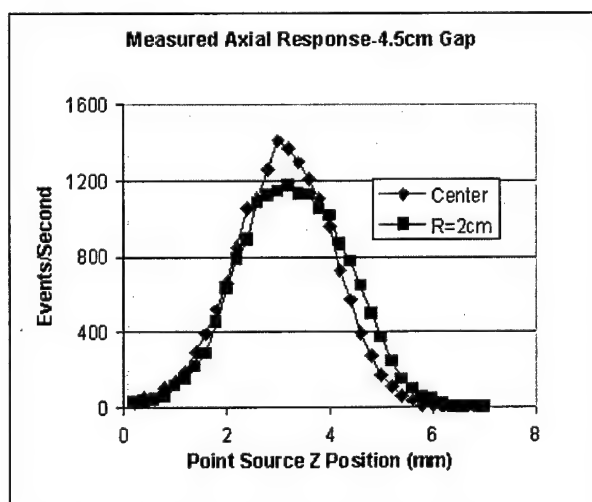


Figure 18: Axial resolution measurements at field center and 2cm radius for 4.5cm

Figure 18 shows a measurement of the axial resolution of the instrument made using a 1mm-diameter point source of  $^{68}\text{Ge}$  and a 4.5mm axial aperture. This aperture can be reduced to provide thinner slices by changing the shielding collimator. In this mode the central axial resolution was measured to be 1.9mm and the resolution at 2 cm radius was 2.3mm.

Figure 19 shows two measurements of scatter fraction for 3.8cm and 6cm tissue equivalent scattering cylinders containing a line source of  $^{18}\text{F}$  at their centers. The measured scatter fraction for the smaller cylinder, .019, is slightly less than that of the first generation instrument as would be expected due to the increased ring diameter.

Figure 20 shows an example of the instrument's performance in an extended object, a high-resolution Micro-Jaczzak phantom. The data are not scatter-corrected. The 1.5mm cold rods are well separated and a hint of the 1-mm rods can be seen near the object center. This is phantom, which is a distribution of cold (non-radioactive) rods of differing sizes in a radioactive background is an extremely rigorous test of instrument image quality.

MMP Generation	Prototype	Final
Point (cps/uCi)	30	56
4.5cm Cylinder (cps/uCi/cc)	204	398

Table 5: Comparison of measured sensitivities for first and second-generation instruments. Both measurements made with 18-F.

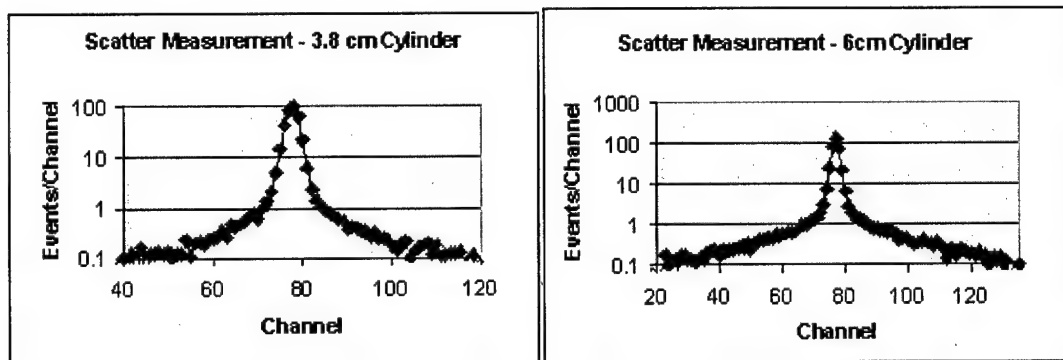


Figure 19: Measurement of scatter distribution from a line source of  $^{18}\text{F}$  at the center of two different sized absorbers. Shown is the sum of the projection data over all angles (i.e., integration of the sinogram over angle). The measured scatter fraction is .019 for the 3.8cm absorber and .048 for the 6-cm absorber.

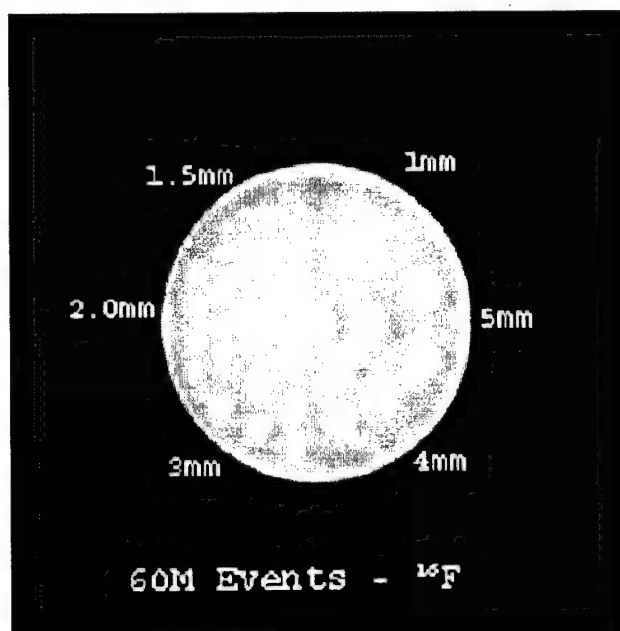


Figure 20: Image of a high-resolution Micro-Jaszczak cold spot phantom (diameter 4.5cm) filled with  $^{18}\text{F}$ . The cold rod sizes are indicated.

#### D. - Animal Studies:

##### a. Animal Studies Carried out by Related DOE Projects Using Instruments:

\*\*\*A DOD-funded project at our institution which is closely related this one is DAMD17-99-1-9555 entitled "Evaluation of Early and Prolonged Effects of Neurotoxicity using Functional Imaging Techniques" (A.L. Brownell, P.I.) Studies of small animals under that program using the instrumentation developed by our effort was part of their aims. During the last three years Dr. Brownell and her co-workers have carried out approximately 100 rat and mouse imaging studies as follows:

1. Sixty  $^{18}\text{F}$ -Fluorodeoxyglucose studies in rats.
2. Forty  $^{18}\text{F}$ -Fluorodeoxyglucose studies in mice.
3. Fifteen  $^{11}\text{C}$  neuro-receptor studies in rats.

Three examples of these studies are shown in figures 21, 22 and 23.

**Fused PET ( $^{18}\text{F}$ -FDG accumulation) and T2 weighted MR images  
after acute 3NP neurotoxicity in rat brain**

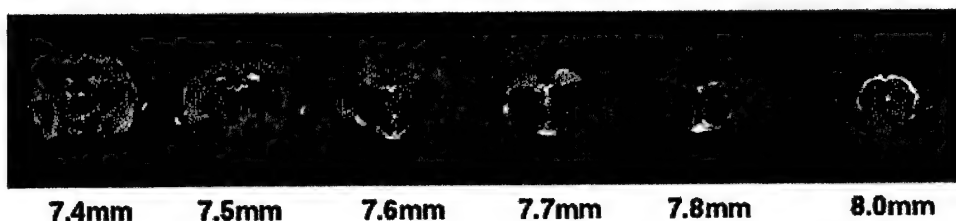


Figure 21: Example of PET study in rat brain registered with MRI.

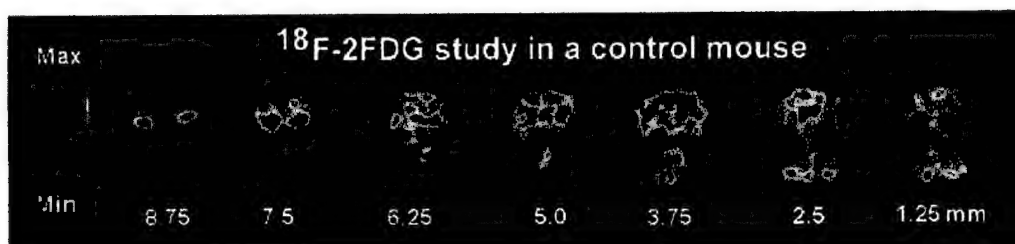


Figure 22: Example of normal mouse brain coronal FDG Images.

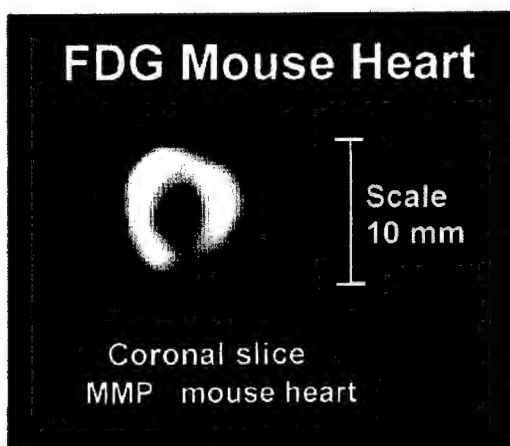


Figure 23: Image of mouse myocardium and enclosed ventricle after injection of FDG.

A particularly interesting example, that of a mouse heart imaged after injection of  $^{18}\text{F}$ -fluorodeoxyglucose, is shown in figure 23. The high-resolution capability of the instruments developed in this project is demonstrated by our ability to see the myocardial wall and ventricle in this very small (25gm) creature.

## b. Bone Metabolism Studies:

During the project a series of preliminary bone metabolism studies were carried out in rabbits and monkeys to demonstrate the use of the imaging instrument for its design purpose. These included three rabbit studies and four monkey studies.

Figure 24 shows a sequence of images taken of the leg of a 2.5 kg rabbit starting below the knee. The tissue sample used (leg) was discarded after a

$^{18}\text{F}$  Sequential Images in Rabbit Leg

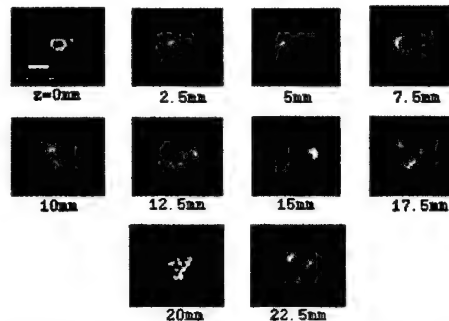


Figure 24: Sequential images, separated by 2.5 min, of lower leg of a 2.5 kg rabbit begun twenty minutes after the injection of 15 mCi of  $^{18}\text{F}$  Fluoride. The sequence moves up the leg toward the knee. Each image was collected for approximately 10 minutes.



Figure 25: Image of lower forearm of 5 kg monkey begun 15 minutes after the injection of 20 mCi of  $^{18}\text{F}$ -Fluoride. Approximately 20 minute imaging time. The periosteal and endosteal surfaces of radius and ulna are clearly seen.

biodistribution dissection study from another protocol.

Figure 25 shows a monkey long bone image (lower forearm) with  $^{18}\text{F}$ -fluoride ion. A relatively low dose was injected (10 mCi). The radius and ulna are both visualized and the endosteal and periosteal surfaces are well separated and clearly seen. To-date we have done two of these preliminary studies in order to establish study parameters and injected dose.

## E. Radioabeling Studies

### 1. Labeling with Iodine:

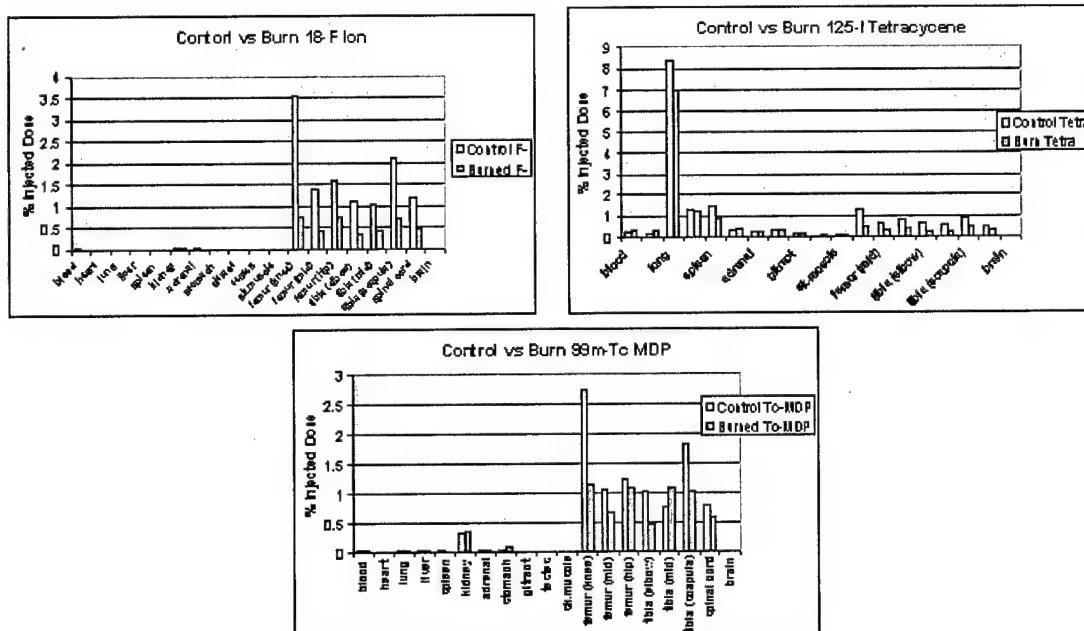


Figure 26: Average organ concentrations at 1 hour post-injection of 125-I tetracycline, 99m-Tc MDP and 18-F fluoride ion in normal and burned rats.

124-I is a potentially useful radioisotope for PET imaging. It is however not readily available commercially at this time. We have been attempting to bring 124-I production on-line at our cyclotron facility under other funding but not established routine production as yet. Anticipating the availability of 124-I we have carried out labeling and biodistribution studies with 125-I, a longer-lived, readily available non-PET isotope of Iodine.

Tetracycline has been labeled with 125-I through exchange labeling using labeled NaI. Its biodistribution was measured in eight control rats and eight rats that had been subjected to a burn model for under another approved project in our laboratory. Rats were co-injected with 125-I tetracycline and 99m-Tc MDP, a bone imaging agent. The animals were sacrificed one hour post injection and dissected. Average organ and structure radioactivity concentrations were subsequently determined by well counting. Also, similar data using 18F-fluoride ion was obtained. The results of these studies are summarized in figure 7. The levels of tetracycline in bone appear adequate for imaging at this early post injection time. Although they lower than either 99m-Tc or 18F-fluoride ion, it should be noted that tetracycline is tracing a much smaller distribution volume, that of newly forming bone.

## 2. 18-F Exchange Labeling:

A series of experiments was carried out to determine if tetracycline could be labeled with 18-F by pre-labeling with non-radioactive iodine and then exchanging for 18-F. This method did not work well and resulted in very low yields.

### 3. $^{11}\text{C}$ Tetracycline Labeling:

We have carried out a series of studies to optimize the production of [ $^{11}\text{C}$ ]-tetracycline. Experiments were carried out using two different chemical precursors, two different radioactive precursors and five different solvents as listed in table 1. In each case several experiments were carried out using variations of the steps listed in figure 1 including different evaporation temperatures and times. The aim was to produce the purest possible labeled tetracycline product.

$^{11}\text{C}$ -methyl iodide ( $[^{11}\text{C}]\text{-CH}_3\text{I}$ ) was used as a starting point for synthesis in all cases. This precursor is routinely produced at our laboratory and is widely used for the synthesis of  $^{11}\text{C}$ -compounds. A system to produce the second precursor, [ $^{11}\text{C}$ ] methyl triflate, from methyl iodide has recently been constructed at our laboratory.

SOLVENTS	CHEMICAL PRECURSORS	RADIOACTIVE PRECURSORS
DMSO	Tetracycline Hydrochloride	$[^{11}\text{C}]\text{-Methyl Iodide}$
Acetonitrile		
Tetrahydrofuran	Tetracycline Freebase	$[^{11}\text{C}]\text{-Methyl Triflate}$
Acetone		
Methanol		

Table 6: Various solvents, chemical precursors and radioactive precursors evaluated of [ $^{11}\text{C}$ ]-Tetracycline.

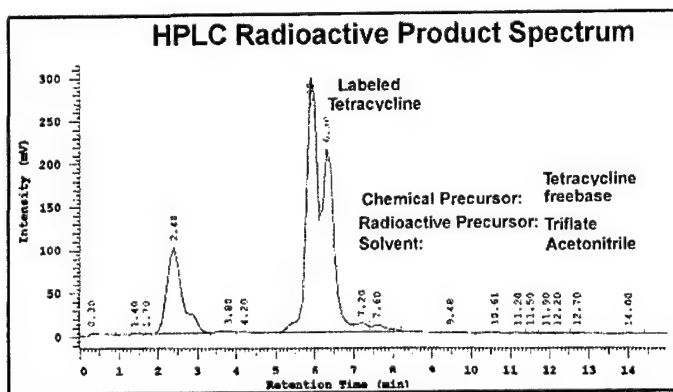


Figure 27: HPLC Radioactive product spectrum. Parameters listed above result in good yield of two labeled tetracyclines

Approximately 40 runs were made and analyzed. Examples of typical HPLC spectra of the product, before purification are shown in figures 27 and 28. The measurements were made using an analytical gradient HPLC system. Figure 27 shows the result for tetracycline

hydrochloride precursor, [ $^{11}\text{C}$ ] Methyl Iodide radioactive precursor and Methanol solvent. The labeled tetracycline yield is low, shows two different labeled tetracycline species, and there are many labeled impurities. This is representative of the poorer results obtained. Figure 28 shows a more successful result using tetracycline freebase, [ $^{11}\text{C}$ ] Methyl Triflate radioactive precursor and acetonitrile solvent. Two labeled tetracycline products above to yield a pure product and predominance of one labeled tetracycline species.

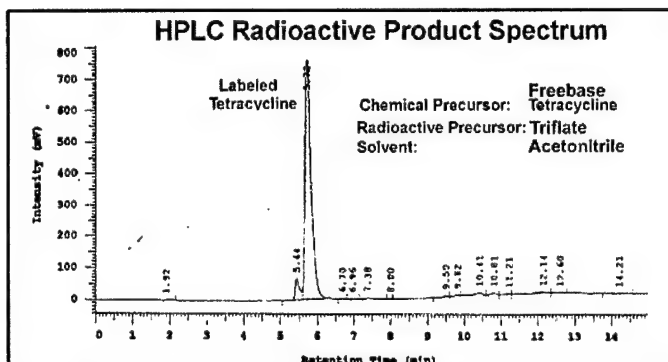


Figure 28: Best case labeling of tetracycline with  $^{11}\text{C}$ . The best combination was freebase tetracycline, [ $^{11}\text{C}$ ]-methyl Triflate, and acetonitrile. These resulted in a large majority of a single labeled tetracycline and low levels of other contaminants.

The optimum production process was determined from these experiments as follows: 1.5mg of tetracycline freebase is dissolved in 400ul of acetonitrile. [ $^{11}\text{C}$ ]Methyl Triflate is collected in this solution at room temperature. The resulting mixture is then heated to  $60^{\circ}\text{C}$  for 1 minute and the tetracycline product separated by preparative HPLC.

#### F. Detector Block Studies for Volumetric Instrument:

Although a single-plane (2-dimensional) instrument is useful in measuring long bones, it is limited to some extent by low sensitivity. An alternative way of stating this is that, in order to sample a large area of the bone, multiple images must be taken sequentially. As part of the development work associated with this

#### LSO Array - 50x1.2x7mm Crystals - 8 PMT's

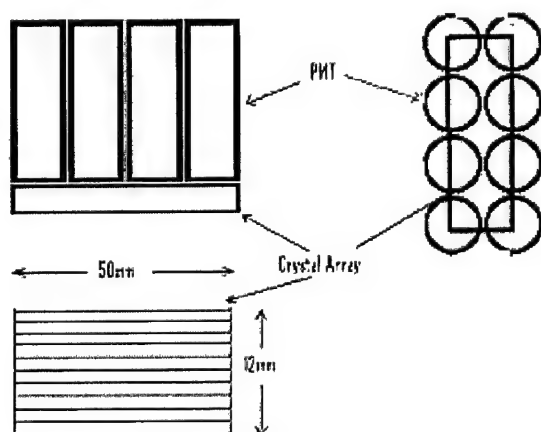


Figure 29. Sketch of 8 phototube block with 50mm axial extent

project we have attempted to design a volumetric (3-dimensional or multi-planar) detector element which could form the basis of a future, higher sensitivity instrument. Most of the electronics and processing software developed in this project could be generalized easily for use with such an instrument. Several bench-top prototypes have been studied and preliminary results from block designs for 1.5cm and 2cm axial extent have been reported in earlier progress reports and in the appended publications. The basis of this design is that light collected and used to identify a given crystal

within a set of transaxial planes, each one of which is equivalent to one data set collected by the single-plane instrument. Our preliminary results indicated that it is possible to separate at least four planes with 15-mm long (z) crystals. This alone would increase the system sensitivity by a factor of four. Further, using coincidence events between planes and volumetric reconstruction could result in as much as a factor of ten increase in sensitivity.

We have more recently constructed and tested prototype blocks having a 5cm axial extent as illustrated in figure 29.

The results illustrate both the potential of the approach and the areas where improvements can (4 PMT rings in a complete system). A sketch of the block is shown in figure 29. Figure 30 shows the axial singles response of the block to a collimated line source of  $^{68}\text{Ge}$  placed at 18 axial positions. This block consisted

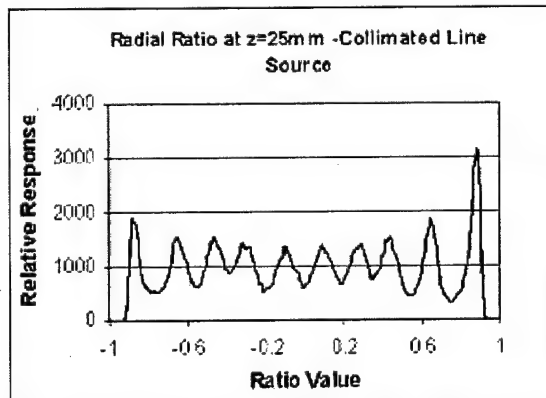


Figure 31. Radial response of 50x1.2x7mm block to a uniform source of  $^{68}\text{Ge}$ . All ten crystals are identified.

windows were used. The amplitude variations in the axial response can be attributed to differences in the block response with position of the source re the phototube array. Also, although the uniformity of resolution is good over the central region of the block, the non-linear response near the detector ends limits the resolution there. Figure 31 shows the radial singles ratio in response to a line source of  $^{68}\text{Ge}$ .

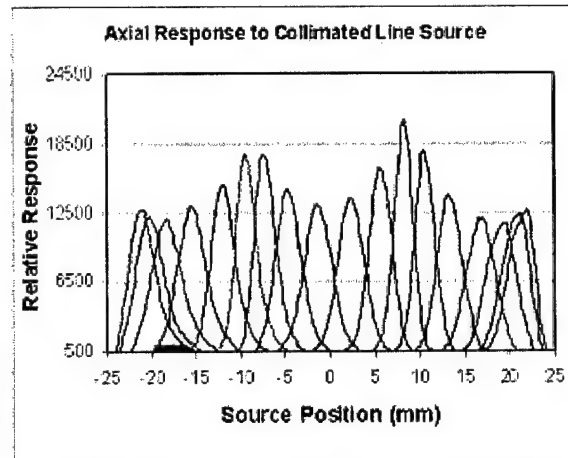


Figure 30. Axial response of 50x1.2x7mm block to a collimated line source of  $^{68}\text{Ge}$  at 2.5mm intervals.

of ten 50 x 1.2 x 7mm crystals with surface preparations similar to those in our single-plane blocks. This block was coupled to eight phototubes, 2.5mm apart along the block. The response was computed from a weighted combination of the lower four phototubes against the upper four. It should be noted that, although phototube gain corrections were used and the signals were subjected to a lower energy threshold no crystal specific energy

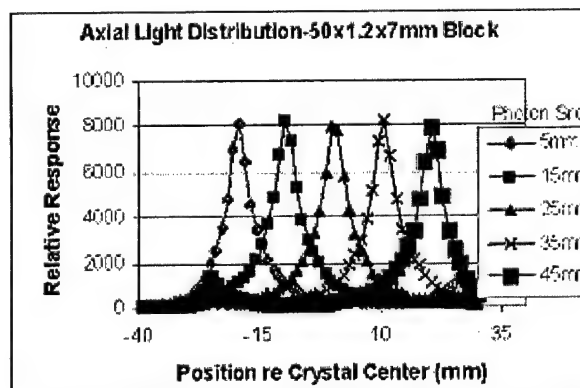


Figure 32. Simulation of axial light output from 50x1.2x7mm LSO block.

Ge. This response was computed by applying the ratio computation described above to the axial sum of the left and right groups of phototubes (see Methods section). All ten crystals are clearly identified. Figure 32 shows a simulation of the axial light distribution for this block. This simulation was carried out using the simulation-package that was developed at our laboratory for detector design studies.

The volumetric detector module design evaluated here has several advantages. The first is that it is relatively simple and inexpensive to fabricate. The second is that it allows for very high imaging resolution without sacrificing light output from the crystal elements. This is a significant problem with systems that attempt to use isolated small crystals or arrays. Our preliminary experience with single-ring systems as well as initial experiments with a volumetric generalizations of the 1-D blocks indicates transaxial and axial performance improves as axial length is increased and therefore that construction of a multi-planar system of the proposed design is feasible. It should be noted that the results of figures 29-31 are for singles and the coincidence resolution will be expected to be higher. The properties of a complete system based on this block design are given in table 7.

Parameter	Volumetric 4-ring System
Detector Diameter(cm)	14.7
LSO Crystals	360
Nominal Size (mm)	1.2x 50x7
# PMT's	144
Block Size	10 crystals x 8 PMT's
Resolution (mm)	1.2 (Cent.) 1.7 (2.5cm)
Sensitivity (cps/uCi)	750
Block Energy Resolution	15%
Time Resolution (2t)	6-12nsec
Gantry Aperture (FOV)	9cm
Axial FOV	4 to 5cm
Max Countrate	50 – 100k trues/sec

Table 6: Design goals for a volumetric system. This system has four PMT rings and crystals with  $z=50\text{mm}$ .

#### **IV. - KEY RESEARCH ACCOMPLISHMENTS:**

1. Demonstration of the feasibility of very high resolution PET imaging in small scale objects.
2. Construction of a working prototype and a second-generation version of a small-scale PET instrument which achieves resolution approaching 1 mm. To our knowledge this is the highest resolution PET device in existence at this time.
3. Specification of PET methodology for the imaging of bone in extremities of primates and demonstrating feasibility.
4. Development of syntheses for labeled tetracycline with several different positron-emitting labels.
5. Extension of the PET instrument design to a volumetric design and experimental verification of feasibility.

#### **V. - REPORTABLE OUTCOMES:**

A number of the studies carried out during this project are reportable and most have already been published. These include:

1. Feasibility of 1 mm PET imaging (published).
2. Simulation of small-scale PET geometries and detector properties (published).
3. Performance evaluation of a small scale PET instrument s (published)
4. Demonstration of feasibility of high resolution (1mm) bone imaging in animal extremities (published).
5. Demonstration of high resolution (1mm) imaging in rat and mouse (published).
6. Development of Tetracycline-labeled radiopharmaceuticals (publication in preparation)
7. Development of volumetric high-resolution Pet design (published).

Please see appendix for details of the published work.

#### **K. - CONCLUSIONS:**

We have met our aims of developing instrumentation, radiopharmaceuticals and methodology for the imaging of bone metabolism in primate and human extremities. We have carried out physical evaluation studies on the instrumentation as well as preliminary animal studies demonstrating feasibility. The final aim of the project was only partially met in that, while demonstrating

feasibility in primates we did not complete the originally proposed bone re-growth study. This study was not completed mainly because of the lack of availability of <sup>124</sup>I, the label with the best imaging properties for bone growth imaging. We plan to continue the pursuit of this aim.

In addition to the main aims of the proposed work we also completed design and experimental studies which resulted in a design for a generalized volumetric version of the instrument developed as part of this project and supported a large body of rat and mouse studies which were supported by a related DOD project in our department.

#### **VII. Personnel Receiving Support from the Program**

1. John A. correia, Ph.D., Physicist	10% (25% effort)
2. Charles Burnham, M.S., Physicist/Engineer	50%
3. Eli Livni, Ph.D., Chemist	10%
4. Anna-Liisa Brownell, Ph.D., Physicist	10%
5. David Kaufman, Engineer	50%

## **VIII. - APPENDIX: Publications List**

1. "Development of a Small Animal Pet Imaging Device with Resolution Approaching 1mm", JA Correia, CA Burnham, D Kaufman, AJ Fischman, *J Nucl Med* 40:285P (1999) Abstr.
2. "Development of a Small Animal Pet Imaging Device with Resolution Approaching 1mm", JA Correia, CA Burnham, D Kaufman, AJ Fischman, *IEEE Trans Nucl Sci* 46:631-635 (1999).
3. "A Pet Imaging Instrument for High Resolution Rat and Mouse Imaging", JA Correia, CA Burnham, D Kaufman, E. Carter, AL Brownell, AJ Fischman, "High Resolution Imaging in Small Animals with PET, MRI and other Modalities: Proceedings", pp 63-64, Amsterdam (1999).
4. "Performance of a Small Animal Pet Imaging Device with Resolution Approaching 1mm", JA Correia, CA Burnham, D Kaufman, AJ Fischman, *IEEE Nuclear Science Symposium and Medical Imaging Conference Record*, M7:pp 1-5 (1999).
5. "Designs for Small Animal PET Systems", Abstr., JA Correia, CA Burnham, D Kaufman, AJ Fischman, *Congress of European Assoc. Nuclear Med*, (Sept, 2000).
6. Design Considerations for Small-Animal PET Devices with Resolution Approaching 1 mm", JA Correia, CA Burnham, D Kaufman, AJ Fischman, , *IEEE Nuclear Science Symposium and Medical Imaging Conference Record*, pp 21:41-45 (2001).
7. " Design of a Volumetric High Resolution Small Animal PET ", JA Correia, CA Burnham, D Kaufman, AJ Fischman, "High Resolution Imaging in Small Animals: Proceedings", pp 187-188, (2001).
8. " An LSO-based detector element for a Multiplanar small animal PET instrument", JA Correia, CA Burnham, D Kaufman, AJ Fischman, *J Nucl Med* 41:56P (2001) Abstr.
9. " Design Studies for a Volumetric High Resolution Small Animal PET ", JA Correia, CA Burnham, D Kaufman, AJ Fischman, " *IEEE Trans Nucl. Sci* ", (2002).

10. 4. "Performance Evaluation of a second-generation single-plane small animal imaging instrument", JA Correia, CA Burnham, D Kaufman, AJ Fischman, *IEEE Nuclear Science Symposium and Medical Imaging Conference Record*, pp M3-166:1-5 (2003).

11. John A. Correia, Charles A. Burnham, David Kaufman, Anna-Liisa Brownell, Alan J. Fischman, "Performance Evaluation of MMP-II: A Second Generation Small Animal PET.", "IEEE Trans Nucl. Sci",, (2003), in press.

12. J.A. Correia, C.A. Burnham, D. Kaufman, A.J. Fischman, "Quasi-continuous Detector Module Design for High-Resolution Small Animal PET", *IEEE Nuclear Science Symposium and Medical Imaging Conference Record*, (2003). In press.

## A PET Imaging Instrument for High Resolution Rat and Mouse Imaging

J.A. Correia, C.A. Burnham, D. Kaufman, E. Carter, A. Brownell and A.J. Fischman  
Massachusetts General Hospital, and Harvard Medical School, Boston, MA 02114

The current frontier in PET instrumentation lies at devices which image at higher resolution over small-scale fields, with the goal of imaging small animals such as monkeys, rats and mice. Small animal imaging presents a situation where positron range effects and sampling are the dominant physical limitations. Annihilation-pair non-collinearity and photon scatter are minimized due to the small dimensions of both instrument and subject. The availability of LSO as a scintillator material for PET leads to several possible approaches to designing detector modules for PET systems having high spatial resolution. The purpose of the work reported here was to design, construct and apply a prototype PET instrument with resolution approaching 1mm using LSO detectors. The approach taken was to design and construct a simple single-plane instrument with as much flexibility as possible in hardware and software implementation. A simple design allows for straightforward modification and adaptation.

The detector array consists of a single ring of 360 1x4.5x5 mm LSO crystals organized into blocks of 12 crystals each viewed by two photomultipliers. Each phototube views two blocks. Thin crystals (0.5 cm) are used to moderate the degradation and non-uniformity of resolution caused by multiple detector penetration at photon incidence angles far from the normal, and minimize blurring due to multiple interaction sites. The choice of thin crystals represents a sacrifice in sensitivity to preserve resolution. The PM Tube signals are processed for timing and position. The coincidence logic uses the timing signal to identify any coincidence event from the central volume of the detector. The 30 linear position signals are DC coupled to the sample-and-hold ADC. Pulse shaping equivalent to a single delay line clipping is used. When a coincidence event is detected the 30 signals are simultaneously sampled and converted to thirty 8 bit words. The deadtime is limited by the time required to transfer, process and store an event in the PC. The preamplifiers, coincidence circuits and digital conversion circuits were implemented using standard logic elements.

The individual blocks were designed based a combination of computer simulations and experimental measurements of the optics for various geometries. The eight interior crystal faces are glued together in a jig with an 80 taper in order to point them toward the ring center. The next two on each side are separated from central crystals and each other by an air gap. The two outside crystals have polished surfaces and a partial reflector isolates them from the adjacent crystals. A reflector is used between blocks. Approximately 1/3 of the light from the peak signals is lost and the energy resolution of the blocks at 0.511 keV is 17%.

Individual crystals are identified using three look-up tables customized for each block. These tables determine if the value of the normalized phototube difference and the energy of the event fall within defined ranges. The third table specifies a normalization factor to adjust for phototube gain differences.

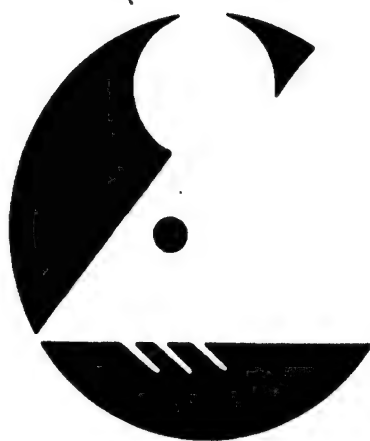
The in plane spatial resolution of the device has been measured to be 1.2 mm at the field center, 1.27 mm at 1 cm radius and 1.55 mm at 2 cm radius using 0.4 mm diameter line sources of 18-F. The axial resolution is variable but has been operated to date at 1.8 mm. The point source sensitivity for a source at the field center has been measured to be 30 coincidences/sec/ $\mu$ Ci using an 18-F point source. The instrument has been applied to the imaging of adult rat brain, juvenile rat torso and adult mouse brain and torso using 18F FDG and fluoride ion as well as several 11-C labeled neuro receptor compounds.

The possibility of PET imaging with LSO detectors at resolution approaching 1 mm has been demonstrated in a prototype single-plane instrument. Resolution degradation is moderated by the use of thin crystals to the degree that objects up to approximately 3.5 cm diameter show only minimal degradation and objects up to approximately 5 cm in diameter maintain off-center resolution below 2 mm. The sensitivity of the instrument is low due to the use of thin detectors to preserve resolution and the need to limit events in a given crystal to a range of energies about the photopeak due to poor light collection from the center of the blocks. This process reduces the efficiency for useful events by 30-60% depending on the energy window-widths chosen.

The most effective use of this instrument in the future is expected to be in imaging mice. Future plans include the characterization and refinement of the detector-block design, further characterization of crystal identification and time discriminator logic, corrections for other physical effects such as attenuation, scatter and randoms in the projection data and design of a multiplane device.

## **HIGH RESOLUTION IMAGING IN SMALL ANIMALS WITH PET, MR AND OTHER MODALITIES**

**Instruments and Applications in Modern  
Biomedical Research**



## **PROGRAM-ABSTRACTS**

**SEPTEMBER 27-29, 1999**

**ACADEMISCH ZIEKENHUIS VRIJE UNIVERSITEIT**

**AMSTERDAM, THE NETHERLANDS**

[authors]

J. CORREIA, C. BURNHAM, D. KAUFMAN, A. FISCHMAN  
Massachusetts General Hospital, Harvard Medical School

[title]

DESIGNS FOR SMALL ANIMAL PET INSTRUMENTS

[text]

We have recently constructed a single plane PET imaging instrument with 1.2 mm spatial resolution. It consists of a 12.4 cm ring of 360 1 x 4.5 x 5mm LSO crystals organized into blocks of 12. Thin crystals were used to minimize photon-multiple-scatter in the detectors. This choice was necessary to obtain high spatial resolution and minimize the effects of inter-detector penetration, but it resulted in a considerable loss of sensitivity. This instrument has been used to image mice and small rats. The 1 mm resolution design-goal was not reached due to difficulties in identifying the outer crystals in the blocks and poor timing and low sensitivity at the centers of some blocks.

A second generation device which acknowledges the above limitations has been designed and is under construction. This device uses 10 1.2 mm crystals per block, each crystal being increased from 5 to 7 mm in depth. The detector ring diameter has been increased to 15 cm. Increasing crystal depth and ring diameter result in a net increase in sensitivity of 1.85, improved crystal identification, and better timing response. Preliminary results indicate that the new blocks will function consistently at 1.2mm resolution. Several designs for multi-planar blocks are also being studied.

[keywords]

PET; Instrumentation; Detectors

[topic]

501

[programme]

SCI

[preference]

EITHER

# Development of a Small Animal PET Imaging Device with Resolution Approaching 1mm

J.A. Correia, C.A. Burnham, *Senior Member IEEE*, D. Kaufman, A.J. Fischman  
Massachusetts General Hospital, and Harvard Medical School, Boston, MA 02114

## Abstract

The work presented here describes progress in the design and construction of a single-plane PET tomograph having spatial resolution approaching 1 mm. The system consists of a 12 cm diameter ring with 360 LSO detectors viewed by 30 photo-multiplier tubes. Thin (5 mm) crystals and a low energy threshold are used. Crystals are identified using both position arithmetic and energy criteria. To-date the system construction has been completed, system tuning carried out and imaging studies begun.

## I. INTRODUCTION

Positron emission tomography (PET) has achieved major successes during the past ten years as a metabolic imaging modality, especially in human and large animal subjects. Instrumentation for use in these regimes has become highly developed and reliable and is used routinely in many laboratories throughout the world. Recently, a number of workers have designed and successfully constructed instruments which image at higher resolution over small-scale fields, with the goal of imaging small animals such as monkeys, rats and mice [1-11].

Small animal imaging presents a situation where positron range effects and sampling are the dominant physical limitations. Annihilation-pair non-co-linearity and photon scatter are minimized due to the small dimensions of both instrument and subject. Theoretical and simulation studies support the idea that spatial resolution on the order of 1mm can be achieved with  $^{18}\text{F}$  and  $^{11}\text{C}$  [12-14]. The availability of LSO as a scintillator material for PET leads to several possible approaches to designing detector modules for PET systems having spatial resolution approaching one millimeter [15].

The purpose of the work reported here was to assess the feasibility of 1mm imaging by designing and constructing a prototype high resolution PET instrument using LSO detectors. The approach taken was to design and construct a simple prototype with as much flexibility as possible in hardware and software implementation. A simple design allows for straightforward modification and adaptation.

## II. SYSTEM DESIGN

### A. General Design

Simulation studies of the geometry including positron range, annihilation non-co-linearity and scatter have been used to develop the design presented here. The approach maximizes the use of software data processing to minimize electronics construction and maintain flexibility. A system block diagram is shown in figure 1.

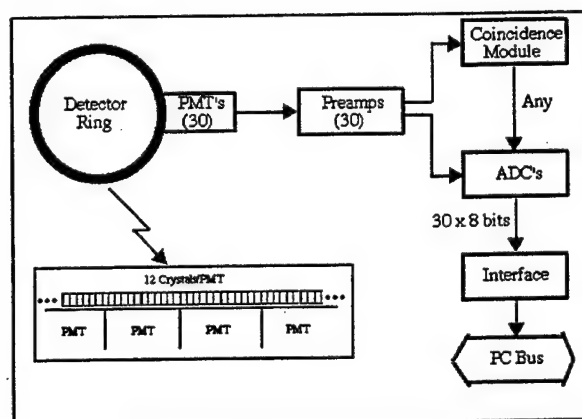


Figure 1: System Block Diagram

The detector array consists of a single ring of 360 1x4.5x5 mm LSO crystals organized into blocks of 12 crystals each viewed by two RCA 647 photomultipliers (PMT's) in a one dimensional implementation of the geometry proposed by Wong [16]. To achieve high resolution, thin crystals (0.5 cm) are used for several reasons; first, the use of thin crystals moderates the degradation and non-uniformity of resolution caused by multiple detector penetration at photon incidence angles far from the normal, and secondly, blurring due to multiple interaction sites is reduced [14]. The choice of thin crystals represents a sacrifice in sensitivity to preserve resolution.

The PM Tube signals are processed for timing and position. The coincidence logic uses the timing signal to identify any coincidence event from the central volume of the detector. The coincidence resolving time of the circuitry is 16 ns. The 30 linear position signals are DC coupled to the sample-and-hold ADC. Pulse shaping equivalent to single

delay line clipping is used. When a coincidence event is detected the 30 signals are simultaneously sampled and converted to thirty 8 bit words. The use of an 8 bit ADC is a compromise between speed and accuracy. The deadtime is limited by the time required to transfer, process and store an event in the computer. The sample update pulse interval is varied to minimize this deadtime. The preamplifiers, coincidence circuits and digital conversion circuits were implemented using standard logic elements. Provision has been made for direct and indirect estimation of random coincidences by measurement of triple coincidence and delayed coincidences.

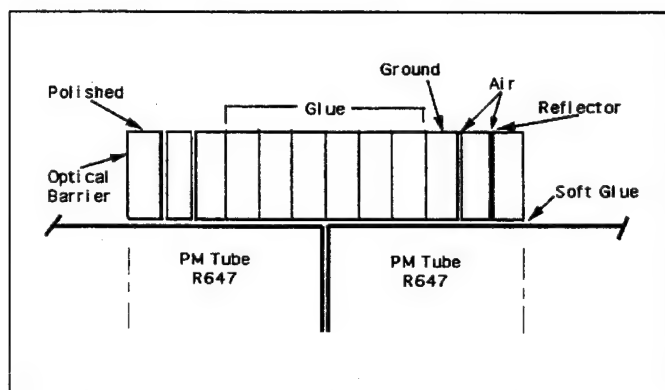


Figure 2. Detail of Block Design showing the various surface preparations used.

### B. Block Design

The individual blocks were designed based on a combination of computer simulations and experimental measurements of the optics for various geometries. The eight interior crystal faces are glued together in a jig with an 8° taper in order to point them toward the ring center. The next two on each side are separated from central crystals and each other by an air gap. The two outside crystals have polished surfaces and a partial reflector isolates them from the adjacent crystals. A reflector is used between blocks. The average fractional signal from each of the crystals for 0.511 keV photons is shown in figure 3. Approximately 1/3 of the light from the peak signals is lost and the energy resolution of the blocks at 0.511 keV is 17% at the center.

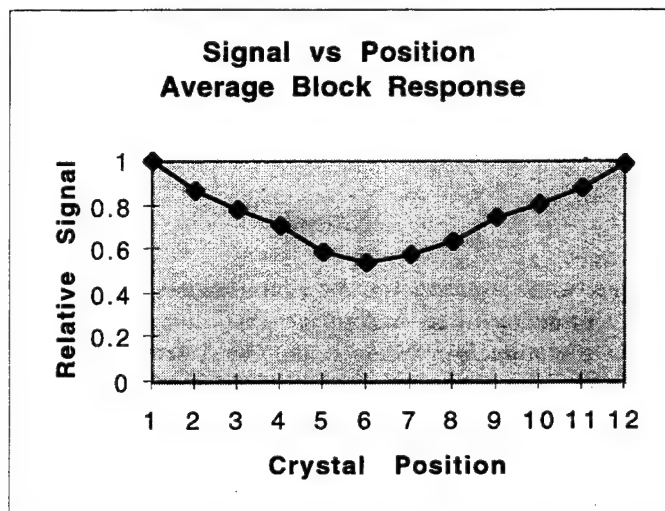


Figure 3: Measured relative crystal signal. Average over 30 blocks.

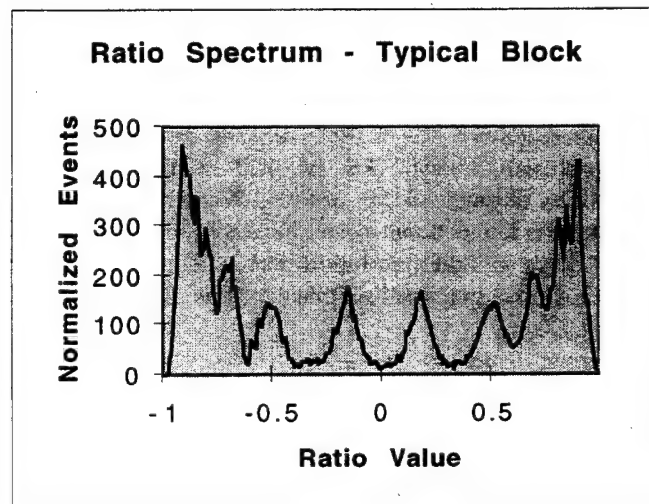


Figure 4.: Ratio from typical block measured with  $^{68}\text{Ge}$ . Photofraction events.

### C. Signal Processing

When a coincidence event is registered by the hardware, the 30 PMT signals are transferred to the computer. The sum of neighboring pairs of PMT signals is computed and if a sum exceeds both neighboring sums and an energy threshold, a block is identified. If three blocks are identified, a triple coincidence is recorded. When exactly two blocks are identified within a data set the processing proceeds to the identification of the individual crystals within each.

The normalized difference ( $R$ ) of PMT signals ( $A$  and  $B$ ) in each block is determined as follows:

$$R = (A - kB) / (A + kB) \quad (1)$$

and if an energy criterion to select only photopeak events:

$$E > E_{\text{threshold}} \quad \text{and} \quad E_{\text{lower}} < E < E_{\text{upper}} \quad (2)$$

is met, a particular crystal is identified, otherwise the event is rejected.

A plot of the  $R$  spectrum from a typical block is shown in figure 4. Figure 5 shows the average bounds for the 30 blocks and figure 6 the individual-crystal energy spectra from a typical block.

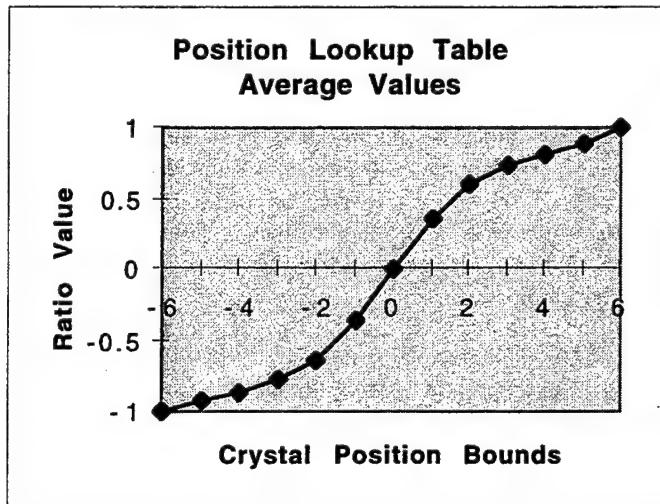


Figure 5: Measured ratios averaged over 30 blocks plotted as a function of ratio with crystal bounds indicated.

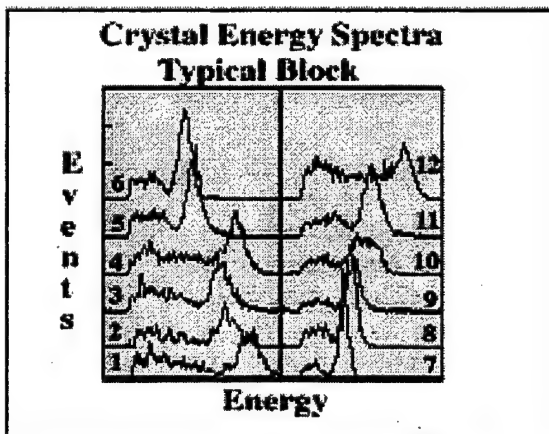


Figure 6: Energy spectra measured from a typical block using a  $^{68}\text{Ge}$  source.

The PMT gains are adjusted such that the maximum signal of each utilizes the full dynamic range of the ADC. A

gain correction ( $k$  in equation 1), implemented via a lookup table, is then applied in the  $R$  calculation to force the ratio at the center of each block to zero.

A given value of  $R$  is associated with an individual crystal within the block via a lookup table specifying the lower and upper levels of the ratio values for that crystal. A good event is recorded if the boundary conditions are met and the phototube-sum, or total energy, signal is within a window derived from the crystal energy spectra. Boundary and energy lookup tables are specified for each block to account for small variations in crystal properties and alignment. The determination of the lookup tables is an iterative process in which a starting set of boundaries are specified from  $R$  plots taken with wide energy windows, then a set of narrower energy windows are specified from the energy spectra and the process repeated until an optimum is reached.

Coincidence data are mapped to a sinogram format for storage, corrected for sensitivity, randoms and attenuation and reconstructed using a standard convolution-backprojection algorithm.

### III. SYSTEM PERFORMANCE

Reconstructed resolution was measured using 0.42 mm diameter  $^{18}\text{F}$  line sources (22 gauge needles). Reconstructions were done with a ramp filter having a cutoff frequency of  $2 \text{ mm}^{-1}$ . Figure 7 shows an example of these measurements and table 1 summarizes the results. The resolution at the center of the field is 1.25 mm and the radial resolution at 2.5 cm radius is 1.75 mm.

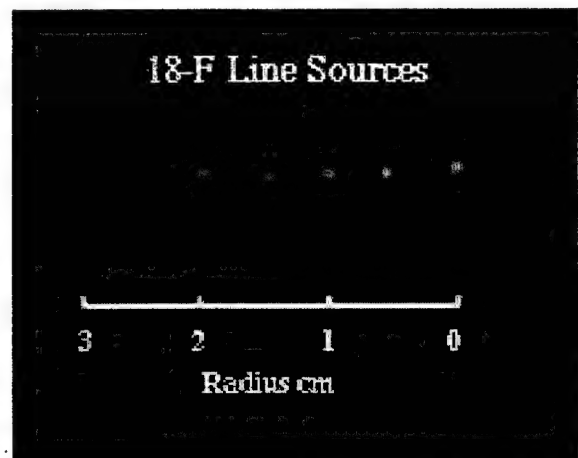


Figure 7: Reconstructed Image of six 0.4mm  $^{18}\text{F}$  line sources, 0.5 cm apart. The scale shown is at 1 cm intervals with the field center at the right.

The axial resolution of the system at the center of the field was measured using a point source of  $^{18}\text{F}$  stepped through the field in 0.1 mm steps. The axial resolution determined by this method was 1.8 mm for the results presented here. In general the axial resolution can be varied by adjusting the distance between two Pb collimator sections shielding the detectors. These collimators consist of two annuli of 5 cm inner radius and 12 cm outer radius. Each annulus is 6 cm long in the axial direction. In addition, the detector ring is shielded on both sides by a 1.25 cm annular Pb plate.

Table 1: Spatial Resolution at Various Field Radii Measured with 0.42 mm Diameter Line Sources.

RADIUS (cm)	FWHM (mm)	FWTM (mm)
0	1.25	2.45
0.5	1.23	2.50
1.0	1.30	2.60
1.5	1.35	2.60
2.0	1.61	3.0
2.5	1.72	3.0

System sensitivity was measured with a centrally located point source of  $^{18}\text{F}$ , a  $^{68}\text{Ge}$  pin source and uniform fields of various diameters containing  $^{18}\text{F}$ . Each uniform field source was approximately 4 cm in z-extent. The results of these measurements are summarized in table 2. The sensitivity listed represents all true coincidences formed by events above a 150 keV energy threshold.

Table 2: Measured sensitivity for cylindrical objects of varying diameter. The reported sensitivity includes all events above 150 keV. The point source sensitivity was measured with an  $^{18}\text{F}$  point and is given in units of cps/uCi.

Diameter (cm)	Sensitivity (cps/uCi/cc)
0.5	3
2.0	40
2.5	69
3.5	145
4.5	204
Point	30 cps/uCi

Preliminary studies in rats have been begun as a means of testing the performance of the instrument under actual laboratory conditions. To-date, only imaging studies at low countrates have been carried out. Figure 8 shows three coronal images of a rat brain after injection of 4 mCi of  $^{18}\text{F}$ -FDG. The collection time for each image data set was approximately twenty five minutes.

Figure 8: Coronal slices, 1.8 mm thick, in rat brain after injection of 4 mCi  $^{18}\text{F}$ -FDG. A: 1 M events. Location: 15 mm forward of inter-aural line. High-uptake structures are the tips of the olfactory bulbs. B: 2.5 M events. Location: 10 mm forward of inter-aural line showing cerebral cortex and striatum. C: 1.0 M events. Coronal image of the posterior of the brain.



#### IV. CONCLUSIONS

The possibility of PET imaging with LSO detectors at resolution approaching 1 mm has been demonstrated in a prototype single-plane instrument. Resolution degradation is moderated by the use of thin crystals to the degree that objects up to approximately 3.5 cm diameter show only minimal degradation and objects up to approximately 5 cm in diameter maintain off-center resolution below 2 mm. The sensitivity of the instrument described here is low due to two factors. The first is the use of thin detectors for the reasons stated above and the second is the need to limit events in a given crystal to a range of energies about the photopeak due to poor light collection from the center of the blocks. This process reduces the efficiency for useful events by 40-60% depending on the energy window-widths chosen.

The measurements of spatial resolution using 0.45 mm diameter needles did not yield 1 mm resolution as at the center of the field as dictated by sampling. This is due in part to poor spatial resolution at the ends of some blocks. This loss of resolution accounts for the fact that the measured resolution is uniform over the central region of the field.

The wide range of signal amplitudes led to poor timing and sensitivity at the centers of some blocks. This effect has not been addressed to-date. Nevertheless the instrument may be effectively used for static imaging situations such as FDG imaging with moderate injected doses and may be useable, with larger injected doses, for some receptor studies. Preliminary tests of the instrument have been carried out in rat brain. The most effective use of this instrument in the future however is expected to be in imaging mice.

Ongoing work includes characterization and refinement of the detector-block design, crystal identification and time discriminator logic. Refinements of corrections for other physical effects such as field non-uniformity, attenuation, scatter and randoms in the projection data are also being

developed. A multiple ring version of this instrument with somewhat larger detector-ring diameter is currently being designed.

## V. ACKNOWLEDGMENT

This work was supported in part by Department of Defense Grant # USAMRAA-DAMD17-98-8511.

## VI. REFERENCES

- [1] Del Guerra A, Scandola M and Zavattini G, "YAP-PET: First Results of Small Animal Positron Emission Tomograph Based on YAP:CE Finger Crystals." *IEEE Transactions on Nucl. Sci.*, 45:3105-3108, 1998.
- [2] Pichler B, Boning G, Lorenz E, et. al., "Studies with a Prototype High Resolution PET Scanner Based on LSO-APD Modules", *IEEE Transactions on Nucl. Sci.* 45: 1298-1302, 1998.
- [3] Cherry SR, Shao Y, Silverman RW, et. al. , "Micropet: a high resolution PET Scanner for Imaging Small Animals, *IEEE Transactions on Nucl. Sci.*, 44:1161-1166, 1997.
- [4] Weber S, Terstegge A, Engels R, et al, The KFA TierPET: Performance characteristics and measurements." *IEEE Nuclear Science Symposium & Medical Imaging Conference Record*, 1117-1120, 1997.
- [5] Watanabe M, Okada H, Shimaza K, et. al., A high resolution animal PET scanner using compact PS-PMT detectors, *IEEE Transactions on Nucl. Sci.* 44: 1277-1282, 1997.
- [6] Bruynodonckx P, Xuan I, Tavernier S, Zhang S, "Performance of a small animal PET scanner based on photosensitive wire chambers, " *IEEE Nuclear Science Symposium & Medical Imaging Conference Record*, 11335-1340, 1997.
- [7] Moses WW, Virador SE, Derenzo SE, et al, "Design of a High-Resolution, High-Sensitivity PET Camera for Human Brains and Small Animals." *IEEE Transactions on Nucl. Sci.*, 44:1487-1491, 1997.
- [8] Lecompte R, Cardorette J, Rodrique S, et. al. "Initial Results from the Sherbrooke Avalanche Photodiode Positron tomograph", *IEEE Transactions on Nucl. Sci.* 43:1952-1957, 1996.
- [9] Bloomfield PM, Rajeswaran S, Spinks T, et. al., "The design and Physical Characteristics of a Small-Animal Positron Emission Tomograph", *Physics in Med. and Biol.*, 40:1105-1196, 1995.
- [10] Seidel J, Gandler WR, Green MV, "A Very High Resolution Single Slice Small Animal PET Scanner Based on direct Detection of Coincidence Line Endpoints", *Journal of Nucl. Med.* 35:p 40P, 1994.
- [11] Tavernier S, Bruynodonckx P and Zhang S, "A fully 3D small PET scanner.", *Phys. Med. Biol.*, 37: 635-643, 1992.
- [12] Correia JA, Burnham CA, Kaufman D, et. al, "Small Animal PET imaging Device - Preliminary Design Study", *J. Nucl. Med.* 38:44P, 1997
- [13] Burnham CA, Elliott JT, Kaufman D, Chesler DA, Correia JA and Brownell G.L, "Single Interaction PET Detectors." *IEEE Transactions on Nucl Sci*, 37:832-835, 1990.
- [14] Burnham C A, Kaufman D E, Chesler D A, Stearns C W, Correia J A, Brownell G L: "A low-Z PET detector", *IEEE Transactions on Nucl Sci* . 37:832-834, 1990.
- [15] Melcher C.L. and Schweitzer J.S, "Cerium doped lutetium oxyorthosilicate: A fast, efficient new scintillator." *IEEE Transactions on Nucl. Sci.* , 39:502-505, 1992.
- [16] Wong WH, Uribe J, Hicks K, et al, "A 2-dimensional detector decoding study om BGO arrays with quadrant sharing photomultipliers." *IEEE Transactions on Nucl. Sci.* NS41: 1453-1457, 1994.

# Performance of Small Animal PET Instrument with 1mm Resolution

J.A. Correia, C.A. Burnham, D.E. Kaufman and A.J. Fischman  
Massachusetts General Hospital, and Harvard Medical School, Boston, MA

## Abstract

A single-plane PET imaging instrument using LSO detectors has been constructed to demonstrate the feasibility of imaging at 1 mm spatial resolution. The performance of this instrument has been evaluated in phantoms and small animals. Measurements presented include spatial resolution, sensitivity, count rate performance, linearity and field uniformity. Examples of several mouse imaging studies are also presented.

## I. INTRODUCTION

The purpose of the work reported here was to evaluate the performance of a single-plane prototype small-animal PET instrument developed at our laboratory. The rationale for developing this prototype was to demonstrate the feasibility of imaging small-scale objects, particularly mice, at 1 mm spatial resolution and further to gain knowledge which will be applied to a second-generation design. The evaluation presented here consisted of measurements of a number of the instrument's physical properties as well as applications to physiological imaging in mice.

## II. SYSTEM DESCRIPTION

The PET imaging system has been described in detail elsewhere [1-2] and therefore, only a brief description will be given here.

The detector array consists of a single ring of 360  $1 \times 4.5 \times 5$  mm LSO crystals [3] organized into 30 blocks of 12, each block being viewed by two photomultipliers (PMT's) in a one-dimensional implementation of the geometry proposed by Wong [4]. The detector-element size limits the spatial resolution. A detector radial dimension of 5mm was chosen to moderate the degradation and non-uniformity of resolution caused by multiple detector penetration at photon incidence angles far from the normal, and to reduce blurring due to multiple interaction sites [5]. This choice represents a sacrifice in sensitivity to preserve resolution.

The crystal interfaces within each block have different treatments to optimize the amount of light reaching the two phototubes. Typically, the light collected at the block center is approximately 1/3 that at the block edge. Outputs of the thirty PM tubes are

processed for timing and amplitude signals. The average crystal energy resolution is 17% at the block center for 0.511 MeV photons.

The coincidence logic uses the timing signal to identify coincidence events from the central volume of the detector with a resolving time of 16ns. Identification of a coincidence event results in the simultaneous sampling and digitization of all the linear PMT signals and their transfer to a PC for processing.

The software identifies a block when the sum of adjacent PMT signals is greater than its neighbors. The normalized difference (ratio) of PMT signals in each identified block is determined. If energy criteria are met, a particular crystal is identified, otherwise the event is rejected. Ratio-boundary and energy lookup tables are specified for each block to account for small variations in crystal properties. Coincidence data are mapped to a sinogram format for storage and subsequently corrected for sensitivity, randoms and attenuation and reconstructed using a standard convolution-back-projection algorithm.

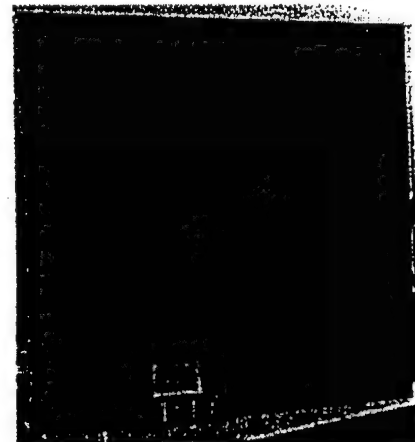


Figure 1: Photograph of PET Imaging System. A 3.5" computer disk is shown for scale.

### III. SYSTEM PERFORMANCE

A number of physical performance measurements have been carried out in order to characterize the instrument's performance. These include both physical studies and preliminary imaging studies in mice. Summaries and specific examples are given in figures 2-11 and the text below. Studies were performed using a large-bore annular Pb collimator having an inside diameter of 7.5cm and a slice gap of 4mm.

The system in-plane spatial resolution was measured using 0.45 mm diameter line sources of  $^{18}\text{F}$  placed at various distances from the center of the imaging field. The sources were filled with low levels of radioactivity to minimize countrates and therefore random coincidences. Images were reconstructed by filtered back-projection using a ramp filter. FWHM and FWTM were measured from profile plots through the reconstructed sources. These measured resolutions were corrected for finite source size by deconvolving the source response function. The results are shown in figure 2a. The resolution at the center of the field is 1.17mm and is 1.66mm at 2.5cm radius. An alternative measurement of the resolution is shown in figure 2b. 1cm x 1cm x 0.75cm-thick polyethylene blocks, each having an array of wells of varying size and spacing, were filled with  $^{18}\text{F}$  solution and imaged. The smallest array, 1.25mm holes at 2.5mm separation is clearly visualized.

The axial resolution at the center of the field was measured by moving a point source of  $^{18}\text{F}$  through the field in 0.1mm steps. The result was 1.75mm FWHM and 3.3mm FWTM as indicated in figure 3.

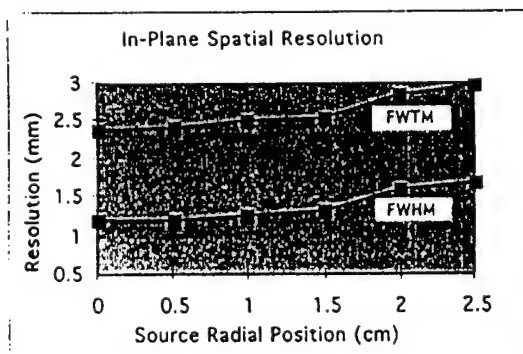


Figure 2a: Spatial resolution vs. field radius measured with 0.45 mm diameter line sources of  $^{18}\text{F}$ . Corrected for finite source diameter. The FWHM and FWTM are shown.

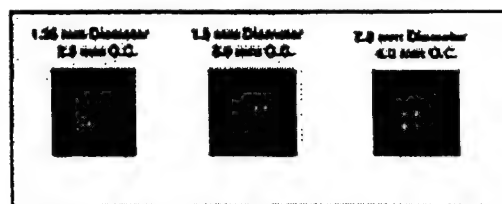


Figure 2b: Spatial resolution phantom consisting of 1 x 1 x 0.75cm polyethylene blocks containing arrays of  $^{18}\text{F}$ -filled wells. The well diameters and spacings are indicated.

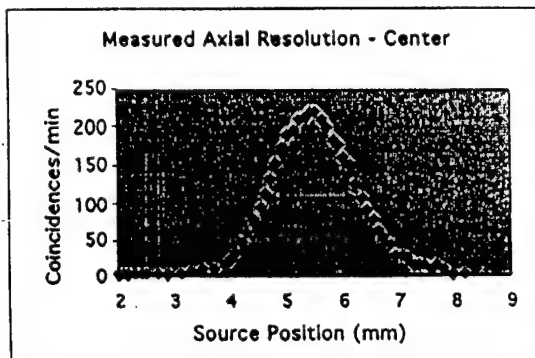


Figure 3: Axial response at field center measured by scanning a point source of  $^{18}\text{F}$  in 0.1 mm steps. The FWHM = 1.75mm and the FWTM = 3.3mm for the collimator gap used in the work presented here.

The system sensitivity was measured using  $^{18}\text{F}$ -filled cylinders of diameters from 0.5 to 4.5cm and a point source at the center of the field. The results for the cylinders are presented in figure 4 along with Monte Carlo simulation results (solid line) for comparison. The point source sensitivity was measured to be 30 cps/uCi.

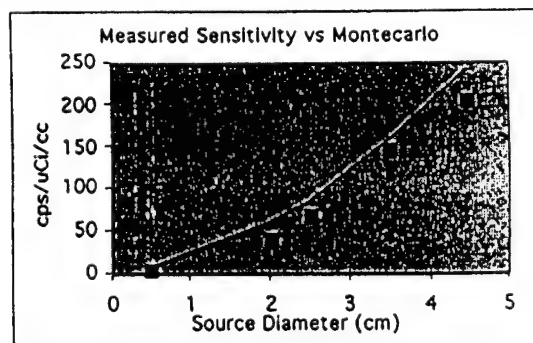


Figure 4: Measured sensitivity for cylindrical objects of varying diameter. The reported sensitivity includes all coincidence events above 150 keV. The solid line represents Monte Carlo simulations of efficiency for 10 cm long cylinders under the same conditions.

The whole-field performance as a function of radioactivity concentration was measured using a 3cm diameter, 1cm long source of  $^{13}\text{N}$  radioactivity. The measurements were made at the coincidence circuit output to eliminate the effects of the computer interface. The single channel events measured were the sum of all PMT timing signals and the coincidence rate measured includes all coincidences from within the central volume of the detector. The trues-data were corrected for randoms but not prompt scatter. Figure 5 shows the results of these measurements. The whole field rate at which randoms=trues is 60k trues/sec and little effect of deadtime was seen up to this rate. The singles/coincidence ratio was acceptably small over the whole range of the measurement.

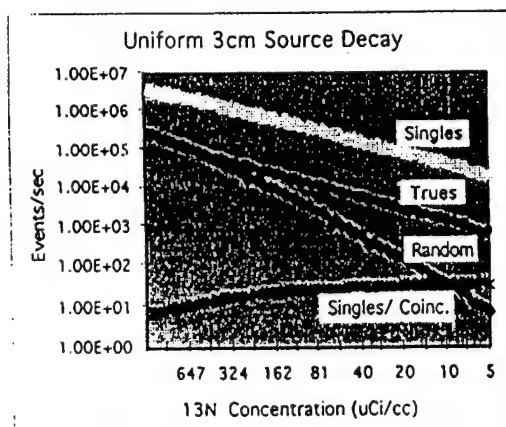


Figure 5: Measured whole field random coincidences, true coincidences, single events and single/coincidence ratio as a function of radioactivity concentration in a 3cm cylindrical object.

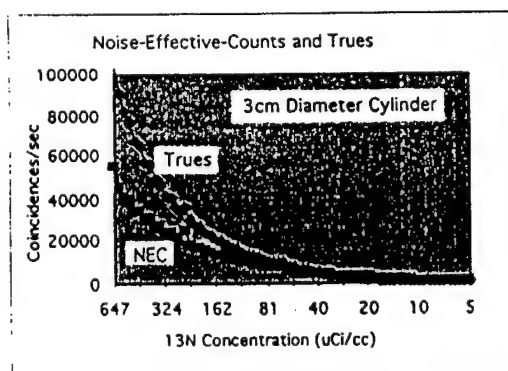


Figure 6: Noise equivalent count rate compared with true coincidence count rate up to randoms = trues for data presented in figure 5.

From these data the noise equivalent countrate as a function of radioactivity in the field was computed incorporating the scatter estimate discussed below. The results, compared to the true coincidence rate, are shown in figure 6.

The linearity of reconstructed activity concentration in small objects was measured over a range of 0.1 to 20 uCi/cc. Arrays of five 3mm diameter cylindrical sources placed at 1cm radius in a 3.5 cm absorber were imaged, reconstructed and relative concentration measurements extracted from ROI's placed over the sources. Figure 7 shows a plot of These results.. The solid line is a linear least squares fit to the measured points. The system is shown to be linear over the range of the measurements with  $r^2 = 0.96$ . Also shown is a sample image from the measurement. The dynamic range of the concentrations in this image is approximately 5 to 1.

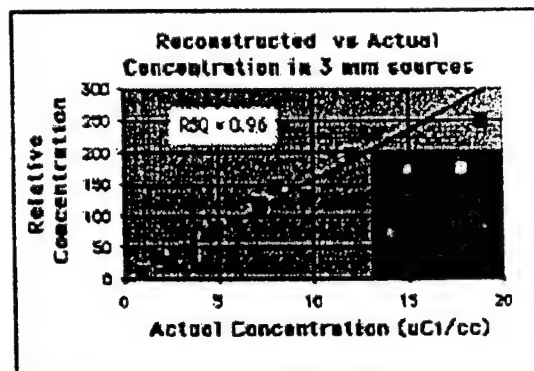


Figure 7: System linearity measured with arrays of five 3 mm diameter cylindrical sources located 1 cm from the field center. The sources were contained in a 3.5 cm diameter cylindrical absorber. The solid line is a linear least squares fit and the inset shows a sample image where the concentration dynamic range is 5 to 1.

The field uniformity of reconstructed data was measured in a 3.5cm-diameter uniform cylinder of  $^{18}\text{F}$  radioactivity. 123 3mm circular ROI's were placed uniformly over the surface of the disk and relative-radioactivity-concentration values extracted. The variation in these values was found to be  $\pm 5.4\%$  (sample S.D.) and randomly distributed in an image with 3.5M coincidence events. The results are shown in figure 8.

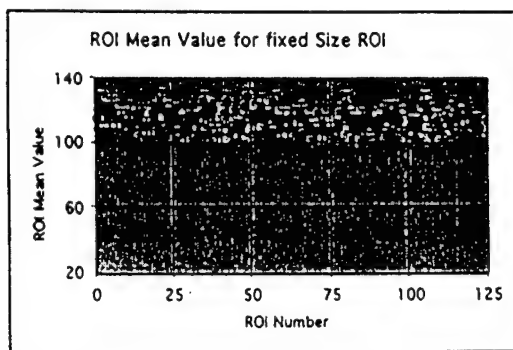


Figure 8: Field uniformity of a 3.5cm diameter cylindrical source sampled with 123 3mm diameter circular ROI's. The error bars are based on the sample standard deviation of  $\pm 5.4\%$ .

The scatter fraction at the center of the imaging field was measured by placing a 0.45mm line source of  $^{18}\text{F}$  surrounded by a 3.8cm diameter cylindrical polystyrene absorber at the center of the field. Data were collected at low countrate to minimize the effects of random coincidences. The sinogram of this object was integrated over all angles and the tails of the resulting data set (outside FWTM) were integrated to

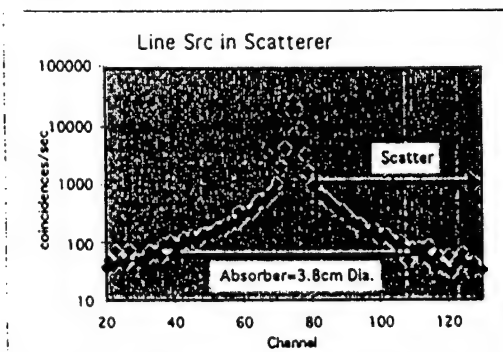


Figure 9: Integral over angle of sinogram of  $^{18}\text{F}$  line source in 3.8cm polystyrene absorber located at field center. Scatter was defined as all events outside the FWTM of the peak. The scatter fraction is 5.7% as compared to a Montecarlo estimate of 7.1%.

provide an estimate of scatter. This was compared to the total integrated counts to give an estimate of the scatter fraction. The result, illustrated in figure 9, is that scatter fraction equals 5.7%. This compares fairly well with the value of 7.1% obtained by Montecarlo simulation.

In order to test the performance of the instrument under actual imaging conditions, a series of mouse imaging studies were carried out. Figure 10 shows a sequence of coronal brain images from a 25gm mouse

taken beginning 40 minutes after the injection of 2mCi of  $^{18}\text{F}$ -FDG. The hemispheres are clearly distinguished and detail at the sub-hemispheric level can be seen. Figure 11 shows selected images from a mouse imaging study collected beginning 30 minutes after the injection of 1 mCi of  $^{18}\text{F}$ -fluoride ion. A high degree of detail may be seen in the bone structure.

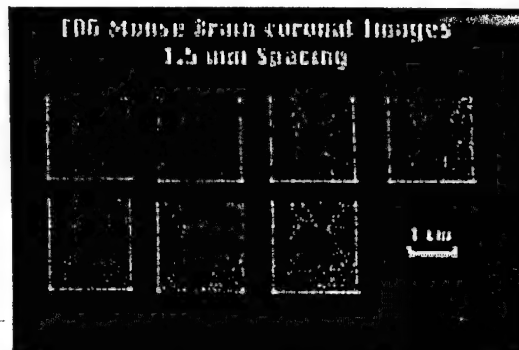


Figure 10:  $^{18}\text{F}$ -FDG Images of mouse brain beginning 40 minutes after injection of 2 mCi of radioactivity. Each image was collected for approximately 20 minutes (1M events).

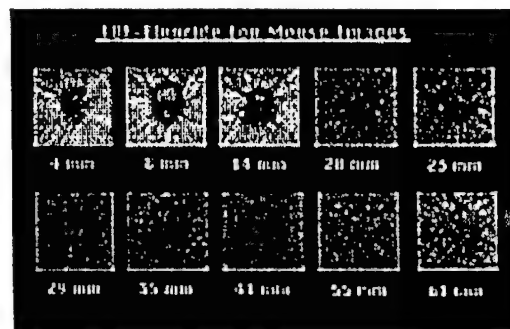


Figure 11: Selected  $^{18}\text{F}$ -Fluoride images of mouse skeleton. Collection was begun approximately 30 minutes after the injection of 1 mCi of radioactivity. 0.25-0.5M events per image. The image positions are measured from the first plane near the nose.

#### IV. CONCLUSIONS

Performance measurements on a single-plane prototype PET instrument have been carried out. The purposes of these measurements were to characterize the instrument and to compile information for the design of a second generation device.

The measured in-plane spatial resolution, after correction for finite source size, is 1.17mm at the center of the field and varies up to 1.66mm at 2.5 cm radius.

These values are poorer than expected based on sampling considerations due in part to poor crystal identification at the block ends. This decreased resolution accounts for the fact that the measured resolution is fairly uniform over the central region of the field. The measured axial resolution of 1.75mm FWHM was obtained for the collimator used in the experiments presented here. By changing the collimator this resolution, as well as the inner diameter of the imaging aperture, may be varied; the range of slice thicknesses being limited on the low end only by system sensitivity and at the upper end by the 4.5mm crystal dimension. An alternative measurement of in-plane resolution, arrays of equi-spaced wells, indicates that high resolution (1.25mm) can be maintained in extended objects.

The system sensitivity for cylindrical objects and a point source at the center of the field agrees well with predictions from Montecarlo simulation although the measured sensitivities are systematically lower by about 20% in the cylinders and by 30% in the point source. The difference for the cylinders may be explained in part by the fact that poor light collection at the centers of the blocks gives rise to timing errors which result in the rejection of some good events. Both effects lead to underestimates of the sensitivity. In the case of the point source, small errors in source position may have a dramatic effect on the measured value and may account for the discrepancy.

The sensitivity is low due to two factors. The first is the use of detectors of limited radial dimension for the reasons stated above and the second is the need to limit events in a given crystal to a range of energies about the photopeak due to poor light collection from the center of the blocks. This process reduces the practical efficiency for useful events by 40-60% depending on the energy window-widths chosen.

The whole-system countrate measurements indicate that the system performs very well at high countrates showing little effect due to deadtime for activity concentrations up to about 800uCi/cc in a 2cm object. This is due in part to the fact that the data set generated is relatively small. The system is randoms limited and the point at which randoms=trues is 450uCi/cc (or alternatively 60,000 trues/sec). The robust behavior of the system in terms of randoms is explained by the highly restricted, single-plane, geometry.

Similarly, the scatter fraction measured with a line source at center-field surrounded by absorber yields a low result of 5.4% due to the restricted geometry. This result agrees fairly well with the 7.1% obtained from Montecarlo simulation.

Measurements of system linearity indicate that the system performs well over a range from 0.1-20 uCi/cc in small extended objects imbedded in absorber. Field

uniformity in objects up to 3.5cm in diameter is about 5.4% (sample S.D.). This figure includes the effects of statistical fluctuations which, for the sizes of object and ROI's used in the measurements and the 3.5M events collected in the data set, is approximately 1.9% at the field center. The distribution of the fluctuations appears random.

The examples of mouse imaging studies shown demonstrate the resolution capabilities of the instrument as well as its limited sensitivity. The instrument may be effectively used for static imaging situations such as 18F-FDG imaging with moderate injected doses and may be useable, with larger injected doses, for some dynamic studies.

The results of the studies presented here have led to several improvements which will be incorporated into a next generation device. These include: improved shielding design; improvements in block design particularly in terms of light output; redesign of the timing discriminator; and an improved PC interface.

## V. ACKNOWLEDGMENTS

This work was supported in part by Department of Defense Grant # USAMRAA-DAMD17-98-8511 and NIH Burn Trauma Center Grant SP50GM21700-22.

## VI. REFERENCES

- [1] Correia JA, Burnham CA, Kaufman D, et. al, "Small Animal PET imaging Device-Preliminary Design Study", *J. Nucl. Med.* 38:44P, 1997
- [2] Correia JA, Burnham CA, Kaufman D, Fischman AJ, "Development of a Small Animal PET Imaging Device with Resolution Approaching 1 mm", *IEEE Transactions on Nucl. Sci.*, 46:631-635, 1999
- [3] Melcher C.L. and Schweitzer J.S, "Cerium doped lutetium oxyorthosilicate: A fast, efficient new scintillator." *IEEE Transactions on Nucl. Sci.*, 39:502-505, 1992.
- [4] Wong WH, Uribe J, Hicks K, et al, "A 2-dimensional detector decoding study on BGO arrays with quadrant sharing photomultipliers." *IEEE Transactions on Nucl. Sci.* NS41: 1453-1457, 1994
- [5] Burnham CA., Elliott JT., Kaufman D., Chesler DA., Correia JA and Brownell G.L, "Single Interaction PET Detectors." *IEEE Transactions on Nucl. Sci.* 37:832-835, 1990.

# Design Considerations for Small Animal PET Devices with mm Resolution.

J.A. Correia, C.A. Burnham, D. Kaufman, A.J. Fischman  
Massachusetts General Hospital, and Harvard Medical School, Boston, MA 02114

## Abstract

We have recently reported a single-plane LSO-based-PET instrument for imaging small animals. The thin detector employed 360 one mm LSO crystals. Images obtained were characterized by resolution approaching the sampling limit of 1mm.

Work directed at extending the performance of this instrument is reported here. A second-generation, single plane device is under construction and preliminary results for a multiplanar instrument have also been obtained.

## I. INTRODUCTION

The purpose of the work reported here was to develop improved designs for the small-animal PET devices which are extensions of the 1 mm prototype PET described previously [1, 2]. This prototype consists of a single 12 cm diameter ring with 360 LSO detectors viewed by 30 photo-multiplier tubes (PMT's). A thin (5 mm) detector with a low energy threshold was used to maximize the detection of single-interaction events and minimize inter-element penetration for non-central lines of response.

Sensitivity is inherently limited by the low stopping power of the thin detector. It is further limited by the fact that the instrument images only a single plane. Although the expected transverse resolution of this system, dictated by sampling, was 1 mm, the actual resolution obtained at center field was approximately 1.2mm. Poor light collection at the center of the blocks resulted in poor timing and loss of low energy signals. Difficulty resolving crystals at the ends of the blocks limited resolution. Despite these limitations applications to small animal imaging demonstrates the capabilities of high resolution imaging and the methodology developed to-date, as exemplified in figures 1 and 2.

Figure 1 shows selected transverse images of <sup>18</sup>F-FDG in the torso of a 25 gm mouse. Structures visible include the kidneys (leftmost image) and bowel (center image). Figure 2 shows a sequence of <sup>18</sup>F-fluoride-ion images of the leg of a 2.5 kg rabbit starting below the knee. The radius and ulna are clearly visualized and the periosteal and endosteal surfaces of the radius are fully separated.

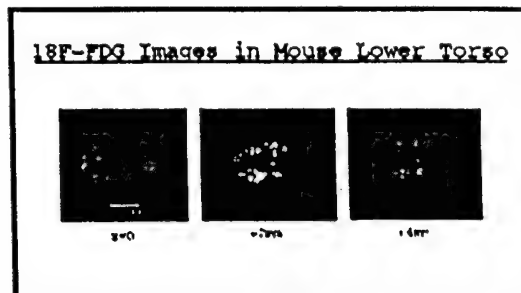


Figure 1: Sequential images of the lower torso in a 25 gm mouse begun 40 minutes after the injection of 2.4 mCi of <sup>18</sup>F-FDG. The plane separation is 2 mm. Each image was collected for approximately 15 minutes.

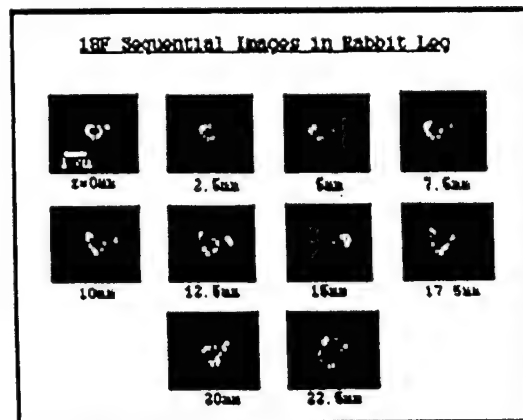


Figure 2: Sequential images, separated by 2.5 mm, of lower leg of a 2.5 kg rabbit begun twenty minutes after the injection of 15 mCi of <sup>18</sup>F-Fluoride. The sequence moves up the leg toward the knee. Each image was collected for approximately 10 minutes.

A second generation, single-plane instrument has been designed and is under construction. The aim, as discussed below, was to improve sensitivity and overcome some of the performance limitations of the prototype.

Although a single plane instrument is useful for some applications, it is limited by low sensitivity. We have therefore attempted to extend our present block design to two dimensions. Such a detector element could form the basis of a future third-generation instrument with substantially higher sensitivity and multi-planar capability.

## II. INSTRUMENT DESIGNS

The characteristics of the second and third generation instrument designs, compared to the completed prototype, are listed in table I. The second generation, single-plane instrument is currently under construction and is nearing completion. A detector for the third generation has been designed, a prototype block constructed and experimental evaluation begun. Both are discussed in more detail below.

### A. Second Generation Single-Plane Instrument

The major changes from the prototype to the second generation, single plane instrument are: (1) fewer crystal-elements per block to improve performance at 1.2mm resolution; (2) crystal elements of 7mm depth to improve stopping power and hence sensitivity and (3) a larger detector-array diameter of 14.7cm with a resulting increase of the number of PMT channels from 30 to 36. The results of imaging studies indicated that the 1mm resolution at the field center as dictated by sampling was not achieved in the prototype due to performance limitations of the 12-crystal detector-blocks. Further some loss of sensitivity was observed due to this limited performance. It was therefore decided to use slightly wider LSO crystals (1.2 mm) in the second generation design. This will limit the maximum resolution to the 1.2 mm achieved with the prototype but will improve the performance of the blocks considerably. Further, it was decided to increase the depth of the crystals from 5mm to 7 mm resulting in a factor of two improvement in sensitivity. Figure 3 shows a schematic diagram of the new detector block. The surface preparations shown in the diagram are similar to those of the 12-crystal block. The faces of the middle six crystals are glued together, the next one on either side is separated by an air gap and the outer two are separated by a translucent Teflon barrier.

Figure 4 shows the ratio spectrum measured from a uniform flux of 511 keV photons. The ratio is computed from the peak signals as:

$$\text{RATIO} = (A - B)/(A + B).$$

	PROTO- TYPE	SECOND GENERATION	THIRD GENERATION
Resolution (mm)	12.3	1.2	14.7
Crystal Depth (mm)	5	7	160
Crystal Size (mm)	1x4.5x5	1.2x4.5x7	1.2x15x7
Resolution (mm)	30	1.2	72
Resolution (mm)	1.16	1.2	1.2
Resolution (mm)	1.6	1.2	1.7
Sensitivity (cps)	35	70	>500

Table I: Properties of prototype, first generation and second generation PET instruments

The end crystals are more clearly resolved than those in the 12-crystal prototype block. Also, the range of pulse amplitudes between the center and edge crystals is lower than the corresponding range in the twelve-crystal block indicating better light collection at the block center. It is expected based on these improvements, that the uniformity of low-energy response will be improved resulting in an additional sensitivity improvement.

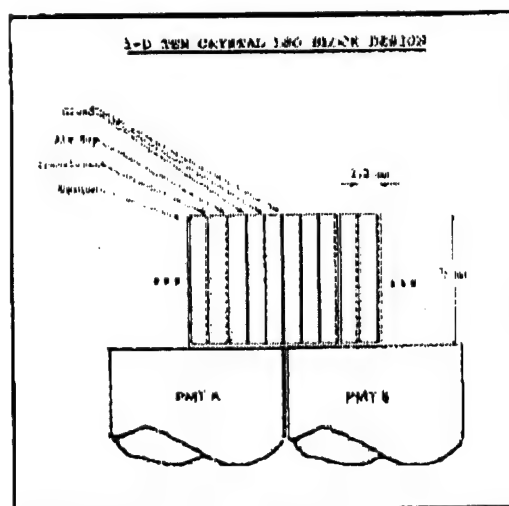


Figure 3: Sketch of 1-dimensional block consisting of ten 1.2x4.5x7mm LSO crystals. The surface treatments of the crystals are indicated.

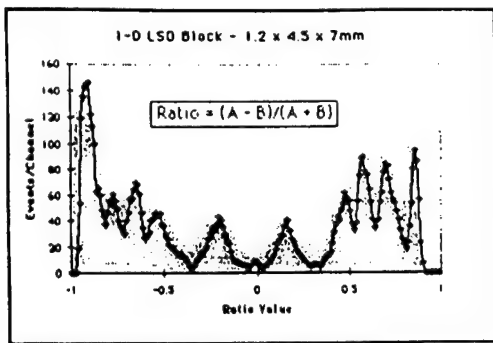


Figure 4: Measured ratio Spectrum for ten-crystal 1D block. The end crystals are more clearly resolved than those in the 12-crystal block. Also, the range of signal amplitudes between the center and edge crystals is lower than the corresponding range in the twelve-crystal block indicating improved light collection at the block center.

The front-end signal processing for the second generation instrument is similar to that of the prototype. When a coincidence event is detected by the electronics, all 36 PMT signals are systematically sampled, digitized and transferred to the computer where individual crystals are identified using four block-specific lookup tables; one each for ratio bounds, energy bounds, PMT-gain-correction and offset. A separate channel is used to collect the total detector singles rate. Thus the majority of processing is done in the computer allowing for a simple, flexible crystal identification procedure.

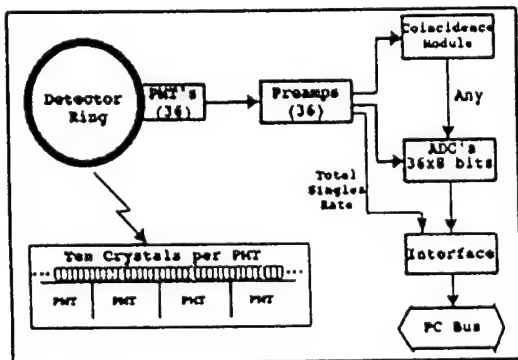


Figure 5: Schematic diagram of front-end processing electronics for second-generation instrument.

The photographs of Figure 6 show progress to date in the assembly of the second generation, single-plane instrument.

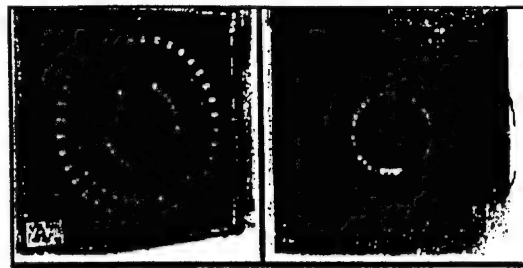


Figure 6: Photographs of the front and rear of the second generation instrument under construction. Left image shows PMT array and right shows the first few LSO blocks in place.

### B. Third Generation 2D Detector Block Design

Although a single-plane instrument is capable of producing high-quality image data, its use is limited by sensitivity. In order to overcome this limitation, we have begun the development of a 2D-detector element with the eventual aim of designing a multiplanar instrument.

Most of the electronics and processing software developed for the single-plane designs was easily generalized for testing the 2D block. The single-plane block design

was extended by increasing the crystal z-dimension from 4.5 to 15 mm and adding an additional row of PMT's as shown in figure 7. The basis of this design is that light collected and used to identify a given crystal within the block also contains information on the vertical (z) position of the interaction within the block. Thus, if the z thickness of the crystals is extended, it is possible not only to identify which crystal gave rise to the interaction but, by a separate computation using the same PMT signals, to obtain the z-coordinate of the interaction. The latter information can then be used to sort events into a set of transaxial planes, each one of which is equivalent to one data set collected by the single-plane instrument. Also, cross-plane coincidences can be used to further increase sensitivity.

The 2D-block was assembled with the same optical boundaries, shown in figure 3, as the 1D block. It was placed symmetrically on four PMT's as shown in figure 7. Measurements were made after adjusting the gains of the PMT's to give the same signal response to a uniform field.

A collimated line source of 511 keV photons, focused across the elements, was used to irradiate the block at several different z-positions with respect to the block-center. The radial ratio was calculated for a 10:1 range of whole-block signal response as follows:

$$\text{RADIAL RATIO} = [(A+C)-(B+D)]/[(A+C)+(B+D)].$$

Examples of these results are shown in figure 8 which gives the measured radial ratio at three different z-positions of the collimated source. All ten crystals are identified in each spectrum.

To assess axial performance, the z-axis ratio was measured for a 10:1 signal range using the same collimated line source. Measurements were made at the center, +/- 1.6mm and +/- 4.8mm and the z-axis ratios computed as follows:

$$Z\text{-RATIO} = [(A+B) \cdot (C+D)] / [(A+B) + (C+D)]$$

Figure 9 shows the results of these measurements. The radial ratio at each source z-position was also calculated and each block-element was clearly identified. At distances greater than 5 mm from the block center the resolution is poorer but the z-ratio still maintains some sensitivity to change.

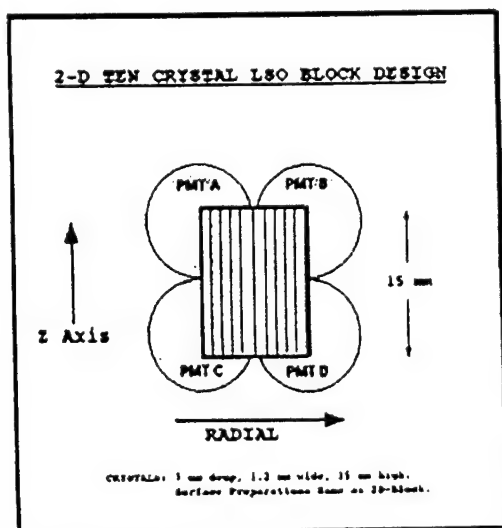


Figure 7: Schematic of ten-crystal volumetric block. The z-dimension is the direction of the plane thickness in the single-ring instrument.

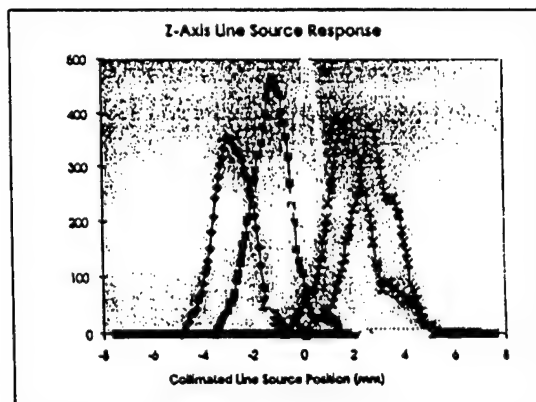


Figure 9: Axial ratio spectrum for a shielded line source of radioactivity placed at -4.8, -1.6, 0 +1.6 and + 4.8 mm with respect to the block center. The z-axis ratio is computed from the four PMT signals as indicated in the text.

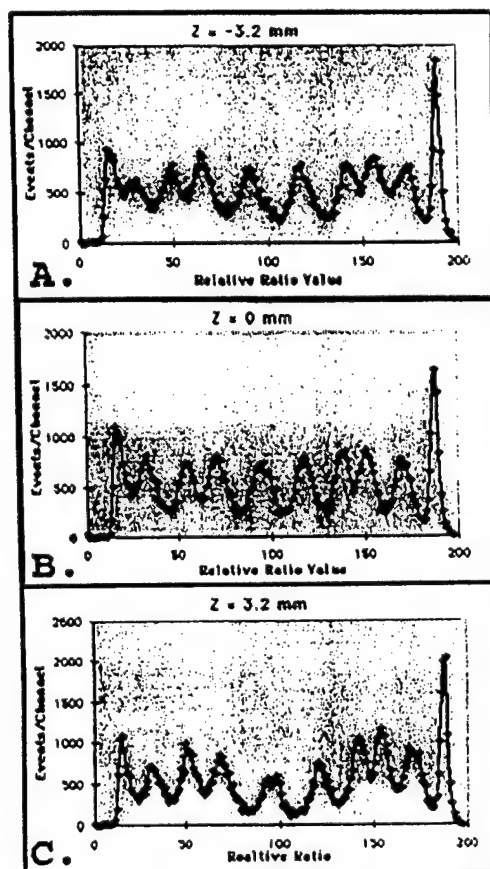


Figure 8: Examples of the 2D block radial ratio for different z-positions of a collimated line source computed from PMT signals as indicated in the text.

### III. CONCLUSIONS

An improved single-plane small animal device has been designed and is under construction. Initial experiments with 10-crystal blocks indicate that crystal identification will be considerably improved compared to our prototype system. Further, improved timing stability, especially for events near the block centers, should result in increased and more uniform sensitivity. The use of etched, rather than polished crystals may lead to further improvement due to higher overall light output.

The detector ring diameter of the second generation instrument has been increased to 14.7 cm in order to offset the increased depth-of-interaction uncertainty due to the thicker detector. Further, the increase in diameter allows the instrument to accommodate larger objects such as a rat torso. The net increase in sensitivity resulting from the thicker detector and larger diameter is approximately a factor of two.

The third generation 2D-detector shows promise as an element for a multiplanar design. Although a uniform light background tended to compress the z-ratio spectra somewhat, the preliminary experimental results presented here indicate that at least 5 planes can be separated over the central 10 mm of the 15 mm detector. Over the same range the 10 crystals making up the block are well separated in the radial dimension.

A design based on a continuous detector in the z-dimension has several advantages. The first is ease of fabrication compared to two-dimensional arrays of individual detector elements. Secondly, the light losses are expected to be lower with the continuous z-detector element due to the higher volume-to-surface ratios of the detector elements. Finally, both the hardware and software developed for the single-plane devices is easily generalized and adapted to the continuous z design.

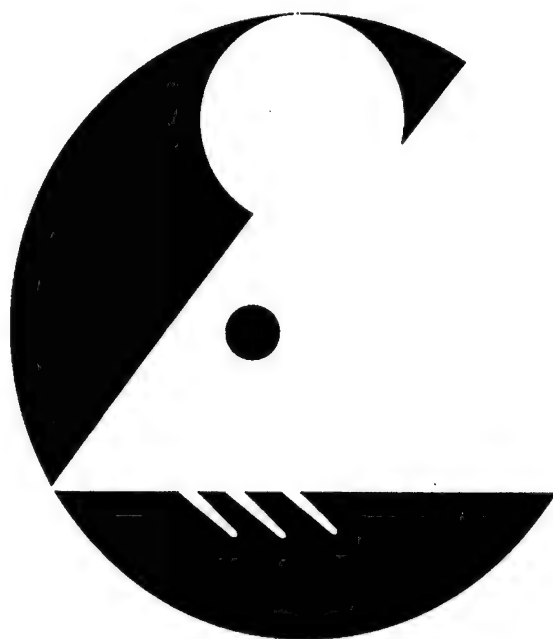
### IV. ACKNOWLEDGMENTS

This work was supported in part by Department of Defense Grant # USAMRAA-DAMD17-98-8511 and NIH Burn Trauma Center Grant 5P50GM21700-22.

### V. REFERENCES

- [1] Correia JA, Burnham CA, Kaufman D, Fischman AJ, "Development of a Small Animal PET Imaging Device with Resolution Approaching 1 mm.", *IEEE Transactions on Nucl. Sci.* 45:631-635, 1999.
- [2] Correia JA, Burnham CA, Kaufman D, Fischman AJ, "Performance of a Small Animal PET Instrument with 1 mm Resolution.", *IEEE Medical Imaging Conf. Conference Record.*, 1999.

# **HIGH RESOLUTION IMAGING IN SMALL ANIMALS:** **Instrumentation, Applications and Animal Handling**



## **PROGRAM-ABSTRACTS**

**SEPTEMBER 9-11, 2001**  
**DoubleTree Hotel**  
**Rockville, Maryland, USA**

# Design of a Volumetric High Resolution Small Animal PET

J.A. Correia, C.A. Burnham, D. Kaufman, and A.J. Fischman. Massachusetts General Hospital and Harvard Medical School, Boston.

**Summary:** We have recently developed two single-plane small animal PET imaging instruments which have spatial resolution of approximately 1 mm. These instruments employed 10 and 12 LSO detector elements respectively per photomultiplier tube. They have served mainly as demonstration prototypes for analog-coded LSO detector block designs but have also been used for numerous rat and mouse imaging studies. They are, however, limited by low sensitivity. By extending the axial length of the elements and adding a second ring of photomultiplier tubes, a high-resolution 2-dimensional block has been implemented. The detector consists of 1.2 mm wide  $\times$  7mm deep  $\times$  15mm high LSO crystals. The crystals are discrete in the radial dimension and continuous in the axial dimension. Event location in both dimensions is achieved using analog position sensing. A ten crystal block has been constructed and tested. Experiments with this detector block have demonstrated 1.2mm radial resolution and approximately 1.6mm axial resolution over the central 12mm of the 15mm detector element. A preliminary design for an instrument based on the 2-dimensional block has been generated. An instrument based on this design results in approximately a ten-fold increase in sensitivity compared to the single-plane designs.

**Introduction:** The purpose of the work reported here was to develop a design for a volumetric small animal PET instrument which is an extension of the prototype single-plane instruments described previously<sup>[1-3]</sup>. To-date a 2-dimensional block has been designed and experimentally evaluated, data acquisition and processing hardware have been redesigned for volumetric data acquisition, a preliminary data acquisition/processing algorithm has been designed and implemented and shielding design for the volumetric system has been undertaken. Both the data acquisition hardware and software are extensions of that previously reported for the single-plane systems.

**Methods and Results:** The surface preparation of the 2D-block is similar to that of the ten crystal 1-dimensional block. The faces of the middle six crystals are glued together, the next on either side is separated by an air gap and a Teflon film separates the outer two. Increasing the crystal axial dimension from 4.5 to 15 mm and adding an additional row of photomultipliers extended the single-plane block design. The basis of this design is that light collected and used to identify a given crystal within the block also contains information on the axial position of the interaction within the block. Thus it is possible not only to identify which crystal gave rise to the interaction but also, by a separate computation using the same photomultiplier signals, to obtain the axial coordinate of the interaction. In order to experimentally evaluate the axial resolution the block was placed symmetrically on four photomultipliers. Measurements were made after adjusting the gains of the photomultipliers to give the same signal response to a uniform field. A collimated line source of 511 keV photons, focused across the elements, was used to irradiate the block at several different axial positions with respect to the block- center. The radial ratio was calculated for a 5:1 range of whole-block signal response as follows:

$$\text{RADIAL RATIO} = [(A+C) - (B+D)] / [(A+C) + (B+D)].$$

Where A, B, C and D are the photomultiplier tube signals.

The z-axis ratio was measured for a 5:1 signal range using the same collimated line source. Measurements were made at the center,  $\pm$  1.6mm and  $\pm$  4.8mm and the axial ratios were computed as follows:

$$\text{AXIAL-RATIO} = [(A+B) - (C+D)] / [(A+B) + (C+D)].$$

The radial ratio at each source z-position was also calculated and each block-element was clearly identified. At distances greater than 5mm from the block center the resolution is poorer but the axial ratio still maintains some sensitivity to change.

The front-end signal processing for the 2D-instrument is similar to that of the single plane devices. Delay line like pulse shaping and leading edge timing are used to process the photomultiplier signals. When a coincidence event is detected, all 72 PMT signals are simultaneously sampled, digitized and then transferred to the computer where individual crystals and event axial position are identified using block-specific lookup tables; one each for ratio bounds, energy bounds, and PMT-gain-correction. Thus the majority of processing is done in the computer allowing for a simple, flexible crystal identification procedure.

The proposed 2D-instrument would consist of 360 LSO crystals organized into a 15cm diameter ring and viewed by two rings of 36 photomultipliers each. The expected spatial resolution, based on preliminary experimental measurements with prototype blocks will be 1.2mm radial at the field center, 1.7mm radial at 2.5cm radius and 1.6mm axial at the field center. The sensitivity will be approximately 500 cps/uCi.

**Conclusions:** The 2D-detector block shows promise as an element for a multiplanar design. Although a uniform light background tended to compress the axial ratio spectra somewhat, the experimental results presented here indicate that at least 5 planes can be separated along the 15mm detector. Over the same range, the 10 crystals making up the block are well separated in the radial dimension.

A design based on a continuous detector in the axial dimension has several advantages. The first is ease of fabrication compared to two-dimensional arrays of individual detector elements<sup>[4]</sup>. Secondly, the light losses are expected to be low, and thirdly, the axial length of the detector can be extended easily.

**Acknowledgments:** This work was supported in part by Department of Defense Grant # USAMRAA-DAMD17-98-8511 and NIH Burn Trauma Center Grant 5P50GM21700-22.

#### References:

- [1] Correia JA, Burnham CA, Kaufman D, Fischman AJ, Performance of a Small Animal PET Imaging Device with 1mm Resolution, IEEE Trans. Nucl. Sci., IEEE Medical Imaging Conf, Conference Record. (1999).
- [2] Correia JA, Burnham CA, Kaufman D, Fischman AJ, Development of a Small Animal PET Imaging Device with Resolution Approaching 1mm, IEEE Trans. Nucl. Sci. 46:631-635 (1999).
- [3] Correia JA, Burnham CA, Kaufman D, Fischman AJ, Design Considerations for Small Animal PET Imaging, IEEE Trans. Nucl. Sci., IEEE Medical Imaging Conf., Conference Record (2000).
- [4] Burnham CA, Kaufman D, Chesler DA, Gregoire MC, Brownell GL MGH Cylindrical PET Operational Characteristics, IEEE Trans. Nucl. Sci. 2: 895-899 (1992).

**AN LSO-BASED DETECTOR ELEMENT FOR A MULTI-PLANAR SMALL-ANIMAL PET INSTRUMENT.**

J. A. Correia\*, C. A. Burnham, D. E. Kaufman, A. J. Fischman,  
Massachusetts General Hospital and Harvard Medical School,  
Boston, MA. (201200)

We have recently constructed two single-plane, small-scale PET instruments using LSO detectors. These instruments have demonstrated the feasibility of imaging at 1mm resolution in small objects but, while they are useful in many imaging situations, single-ring detectors are limited in sensitivity due to the small geometric solid angle subtended. To overcome this sensitivity limitation, we have generalized the detector block design used in the single-plane instruments by extending the axial dimension to form a multi-planar block. The design criteria were: (1) 1.2 mm spatial resolution at the field center; (2) simplicity and ease-of-fabrication of detector elements; (3) minimization of light losses in the small detector element. The multi-planar block design consists of ten LSO crystals, 1.2mm radial  $\times$  7mm thick  $\times$  15mm axial, attached at the 7 $\times$ 15mm faces. The central six crystals are glued together, the next one on either side of center is separated by an air gap, and the outer one on either side by a partial reflector. The detector block is centered on an array of four PMT's. The PMT signals are used in several combinations to identify which crystal scintillated and where along the 15mm (z) dimension the scintillation took place. Preliminary experimental results indicate that, for 511 keV photons, the individual crystals can be clearly identified at z positions from 0 to  $\pm 6$  mm re the detector-element center and that the z-dimension can be binned into at least 5 planes over the central 12 mm of the detector block. Light reflection at the crystal ends prevents identification of events for  $z \pm 6$  mm in the current design. In addition to improving sensitivity, the block described here may provide opportunities for improved radial sampling, and hence, higher resolution. A multi-planar small-animal PET instrument based on this block is currently being designed. This work was supported in part by Department of Defense Grant #USAMRAA-DAMD17-98-8511.

### Proceedings of the SNM 48<sup>th</sup> Annual Meeting

values yielded a Pearson correlation coefficient of 0.82 ( $p = 0.002$ ).

**Conclusion:** The results show a significant positive correlation between radioactivity values obtained with PET and storage phosphor autoradiography used as gold standard. Thus, the developed PET system is suitable for *in vivo* receptor binding studies in small laboratory animals.

# Design Studies for A Volumetric High Resolution Small Animal PET.

J.A. Correia, C.A. Burnham, D. Kaufman, A.J. Fischman  
Massachusetts General Hospital, and Harvard Medical School, Boston, MA 02114

## Abstract

We have developed two LSO block detectors for single-plane small animal PET instruments which have spatial resolution of approximately 1 mm. They have served mainly as demonstration prototypes but have also been used for numerous rat and mouse imaging studies. By extending the axial length of the detector element from these systems and adding a second ring of photomultiplier tubes, a high-resolution 2-dimensional block using analog position sensing in both the radial and axial dimensions has been implemented. It consists of ten 1.2 mm wide x 7mm deep x 20mm high LSO crystals that are discrete in the radial direction and continuous in the axial direction. An instrument based on this design results in a substantial increase in sensitivity. Experiments with this detector element have demonstrated 1.2-mm radial resolution and approximately 1.6-mm axial coincidence resolution over the central 15mm of the 20mm high block element. A preliminary design for an instrument based on the 2-dimensional block has been evaluated by simulation studies.

## I. INTRODUCTION

The purpose of the work reported here was to develop a design for a volumetric small-animal PET instrument, which is an extension of the prototype single-plane instruments, described previously [1, 2, 3]. This generalization is achieved by extending the axial dimension of the crystals and adding a second ring of photomultiplier tubes (PMT's). Analog coding in both the radial and axial dimensions, based on the signals from four PMT's viewing each detector block, is used to identify the position of each event.

Previously reported experiments with a 1.2x5x15mm block have demonstrated the feasibility of a 2-dimensional detector element [3]. In order to increase sensitivity, both crystal thickness and axial extent of have been increased resulting in a block having dimensions 1.2 x 20 x 7mm.

We have been able to achieve spatial resolution of approximately 1 mm in single-plane systems by exploiting the fact that, in a thin detector, a large fraction of the detected events are single interactions. Extending the dimensions of the elements to improve sensitivity also increases the multiple interaction rate. We have attempted to explore the effects of such multiple interactions by simulation and to experimentally evaluate the performance of the larger block. In addition, the sensitivity and scatter performance of a system based on the larger block has been evaluated by Monte Carlo simulation and data acquisition and processing hardware for the single plane systems has been generalized for operation with the volumetric system. The details of these studies are presented in the following sections.

## II. BLOCK DESIGN AND PERFORMANCE

The single-plane block design was generalized by increasing the crystal z-dimension from 4.5 to 20 mm and adding an additional row of PMT's as shown in figure 1.

The crystal surface preparations are similar to those of the 10 and 12-crystal 1-dimensional blocks previously constructed. The faces of the middle six crystals are attached using silicon glue, the next one on either side is separated by an air gap and a partially translucent Teflon barrier separates the outer two.

The basis of the volumetric design is that light collected and used to identify a given crystal within the block also contains information on the axial position of the interaction within the block. Thus, if the axial dimension of the crystals is extended, it is possible not only to identify which crystal gave rise to the interaction but also, by a separate computation using the same PMT signals, to obtain the z-coordinate of the interaction. The latter information can then be used to sort events into a set of transaxial planes, each one of which is equivalent to one data set collected by the single-plane instrument. Also, cross-plane coincidences can be used to further increase sensitivity.

The block was placed symmetrically on four PMT's as shown in figure 1. The radial response was then determined from the PMT signals as follows:

$$R\text{-RATIO} = [(A + Cg_1) - (B + Dg_2)] / [(A + Cg_1) + (B + Dg_2)]$$

and the value of this quantity used to identify the crystal in which an interaction took place. In a similar manner, the axial response was determined from the PMT outputs as:

$$Z\text{-RATIO} = [(A + Bg_3) - (C + Dg_4)] / [(A + Bg_3) + (C + Dg_4)]$$

and used to determine the axial location of the interaction. The gain factors,  $g_i$ , were determined from the response to a uniform photon flux and were chosen to force symmetry about the central axes of the block. This has the effect of minimizing pincushion distortion and other effects.

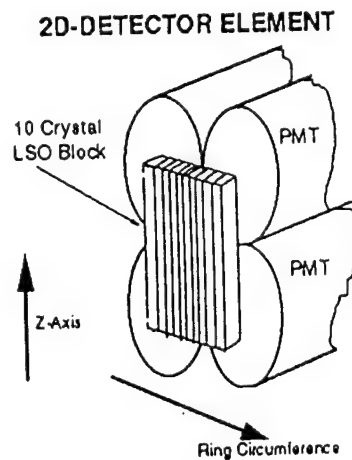


Figure 1: Schematic of ten crystal volumetric block.

Optimum energy and radial ratio lookup tables for crystal identification were determined by iterative adjustment using data from uniform field measurements. The fifty photopeak centroids, from which individual crystal energy bounds were determined, are shown in figure 2.

Two experiments were carried out to evaluate the response of the detector element to single 511 keV photons. To evaluate radial response, the block was irradiated with a uniform  $^{68}\text{Ge}$  source and the radial ratio computed over five z-ranges centered at  $z = -6\text{mm}$ ,  $-3\text{mm}$ ,  $0\text{mm}$ ,  $3\text{mm}$  and  $6\text{mm}$  with respect to the block center. Approximately 500k raw events were collected at each position and the energy bounds used for each crystal were 80 to 120% of the photopeak centroid. The results of this experiment are shown in figure (3). All crystals are clearly identified at all z positions.

In the second experiment, to assess axial response, the block was irradiated with an axially collimated line source

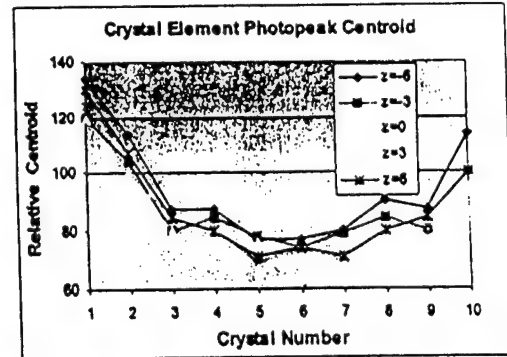


Figure 2: Relative location of 511 keV photopeak centroids as a function of crystal number for narrow z-ranges about the specified values.

1mm wide at seven axial positions from  $-9\text{mm}$  to  $+9\text{mm}$  with respect to the block center. Approximately 300k raw events were collected at each position using the same crystal energy ranges and bounds. No correction was made for finite source width. Figure 4 shows the results of these measurements.

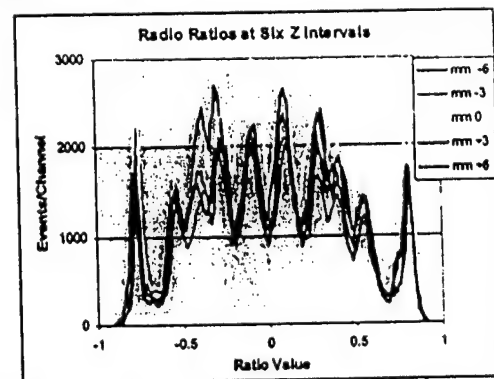


Figure 3: Examples of the 2D block radial ratio for a uniform source computed from PMT signals as indicated in the text.

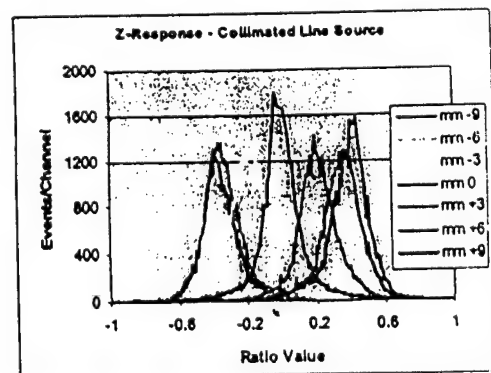


Figure 4: Block axial singles response using a collimated line source. Inter-source distance = 3mm. No source correction applied.

The effects of multiple interactions on the block performance were evaluated by Monte Carlo simulation. Histories of 60,000 photons of 511 keV energy normally incident on the center of a continuous block of LSO material 10 cm long 2 cm high and of depths varying from 0.1 to 1 cm were generated. The fraction of single- and multiple interaction events as well as the centroid of energy deposition for all interactions were determined as

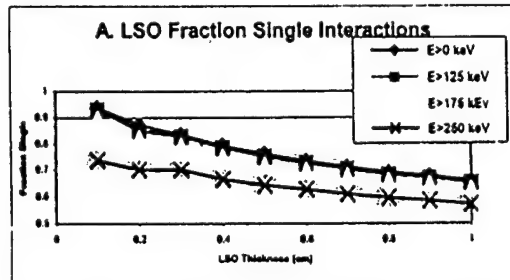


Figure 5: Monte Carlo simulation of single interactions in LSO.

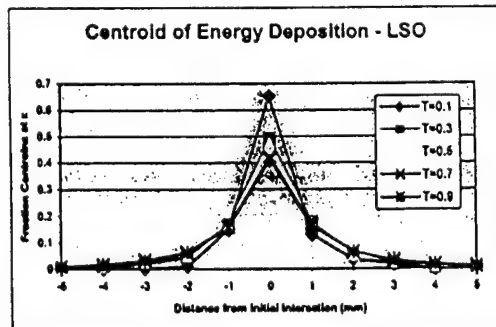


Figure 6: Monte Carlo simulation of centroid of energy deposition for normally incident 511 keV photons on LSO of various thicknesses (T). Binned in 1mm intervals.

a function of detector thickness for energy thresholds of 0, 125, 175 and 250 keV. Figure 5 shows the single interaction rate resulting from these simulations. Extending the detector thickness from 5 to 7mm results in a modest increase of about 10% in the multiple interaction rate with a corresponding decrease in the single interaction rate. Figure (6) shows the distribution energy centroids, analogous to the center of brightness in the scintillator, binned in 1mm intervals about the direction of incidence of the photon beam. Increasing the detector thickness from 5mm to 7mm results in a decrease of approximately 10% in the number of events

having an energy centroid within 1mm of the interaction site.

### III SYSTEM DESIGN

A volumetric system design based on the block described above has been generated. Preliminary design parameters for this system are given in table 1.

PARAMETER	VALUE
Diameter(cm)	14.7
LSO Crystals	360
Crystal Size(mm)	1.2x20x7
Detector Element Width	72
Scintillation Layer Thickness	1.2
Scintillation Layer Material	1.7
Scintillation Layer Density	1.6
Scintillation Layer Color	>300

Table 1: Specifications for Volumetric Instrument.

The system sensitivity for several geometries based on the above-described block was determined by Monte Carlo simulation. Systems with detector element sizes of 1.2x15x5mm (assuming a 1.2 cm useable z) and 1.2 x20x7mm (assuming a 1.5 cm usable z) were studied in comparison with our single plane systems. Sensitivity and scatter fraction were determined for 10 cm long cylindrical objects varying in diameter from 1 to 5 cm as well as point sources were simulated. Each simulation consisted of 40 million histories.

Figure 7 presents the results for cylindrical sources and Table II gives similar results for point sources. For the proposed system having 1.2x20x7mm detector elements and assuming that 1.5cm is the useful axial width, the gain in sensitivity compared our single-plane system will be approximately 15 for a 4cm mouse-sized object. Similarly the point sensitivity gain (table II) will be approximately 10.

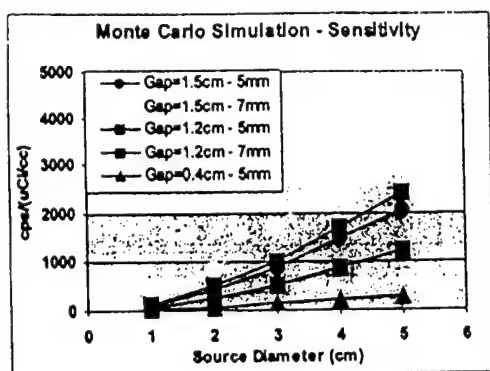


Figure 7: Monte Carlo simulation of system sensitivity for cylinders. Several combinations of axial gap and crystal thickness including single plane system are shown.

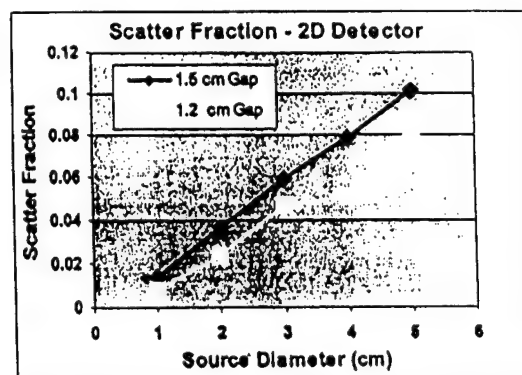


Figure 8: Monte Carlo simulated scatter fraction for two possible z-gaps.

z (mm)	cps/uCi 5mm LSO	cps/uCi 7mm LSO
0.4	35	90
1.2	129	255
1.5	174	344

Table II: Point source sensitivity for various LSO detector-element sizes.

The fraction of scattered events from the same simulation set is presented in figure 8 for 10cm long cylindrical objects. For mouse-sized objects, the scatter fractions vary between 0.06 and 0.08 for the geometries considered.

The front-end signal processing for the volumetric instrument is a generalization of that used in our single-plane systems. When a coincidence event is detected by the electronics, all 72 PMT signals are systematically sampled, digitized and transferred to the computer via a buffered PCI interface. The individual crystals are then identified using block-specific lookup tables; one each for ratio bounds, energy bounds and PMT-gain-correction. A separate channel is used to collect the total detector singles rate. Thus the majority of processing is done in the computer allowing for a simple, flexible event- localization procedure.

#### IV. CONCLUSIONS

LSO is a well-suited material for use in small animal PET imaging instruments where the amount of source scatter is relatively low moderating the need for high-energy resolution. The high light output of LSO also allows for the design of simple detector modules based on light sharing.

The 2D LSO block discussed here, consisting of ten 1.2x20x7mm crystals, shows promise as an element for a multi-planar design. The sampling in the axial dimension is continuous. The preliminary experimental results presented here indicate that 5-7 planes can be separated over the central 15 of the 20mm detector. The axial singles resolution, without correction for finite source extent is approximately 2.3mm at the block center. This should yield a coincidence axial resolution of approximately 1.6 mm. The resolution in the radial dimension is sampling-limited by the crystal size of 1.2mm. All ten crystals are well separated over the central 15mm of the block. Light losses from the center crystals result in a variation of photopeak centroid location of approximately 40%. Although the variation radially is much stronger than that in the axial dimension it is still necessary to invoke a two-dimensional energy criterion to clearly identify both crystal and z-coordinate.

The basis for the design of the original single-plane systems was that the use of a thin detector and a low energy threshold would yield a high fraction of single-interaction events. A thin detector however results in low coincidence detection efficiency. In the current design the thickness of the detectors has been increased from 5 to 7mm which doubles coincidence sensitivity but also increases the fraction of multiple-scatter events. The simulation studies presented here indicate that the effect

of such increased multiple interactions will be relatively small (about a 10% increase in multiple scatter events and a 10% decrease in the number of events depositing their energy within 1mm of the interaction site for normally incident photons). The fact that the radial ratio spectra show some buildup of background toward the center of the crystal, manifested as a slight bowing of the spectra, may be attributable to increased multiple scatter events. This distortion was not observed with a 5mm block evaluated earlier. Nonetheless the individual crystals are clearly separated indicating that this is not a major effect.

Simulations for the chosen geometry indicate that gains of about 15-fold in sensitivity will be achieved in extended objects while maintaining an acceptably small scatter fraction. Such an increase will allow for substantially higher quality static and dynamic studies than have been possible with the single-plane prototype systems.

A design based on a continuous detector in the z-dimension has several advantages. The first is ease of fabrication compared to two-dimensional arrays of individual detector elements. Secondly, the light losses are expected to be lower with the continuous z-detector element due to the higher volume-to-surface ratios of the detector elements. Finally, both the hardware and software developed for the single-plane device are easily generalized and adapted to the continuous z design and are relatively simple.

The approach presented is limited by reduced response to changes in axial dimension near the ends of the block. While it may be possible in principle to moderate end effects by using a probabilistically based algorithm for axial position, it would be very difficult in practice since, effectively, only two measurements, the radial sums of PMT pairs are available. An alternative approach is to lengthen the crystals axially and add one or more additional rows of PMT's.

with Resolution Approaching 1 mm", IEEE Nuclear Science Symposium and Medical Imaging Conference Record, pp 21:41-45 (2001).

## VI. ACKNOWLEDGEMENTS

US Department of Defense Grant # USAMRAA-DAMD17-98-8511, and NIH Burn-Trauma Center Grant 5P50GM21700-22.

## V. REFERENCES

- [1] Correia JA, Burnham CA, Kaufman D, Fischman AJ, "Development of a Small Animal PET Imaging Device with Resolution Approaching 1 mm.", *IEEE Transactions on Nucl. Sci.* 45:631-635, 1999.
- [2] Correia JA, Burnham CA, Kaufman D, Fischman AJ, "Performance of a Small Animal PET Instrument with 1 mm Resolution." *IEEE Medical Imaging Conf. Conference Record.* 1999.
- [3] Correia JA, Burnham CA, Kaufman D, Fischman AJ, Design Considerations for Small-Animal PET Devices

# Performance Evaluation of MMP-II: A Second Generation Small Animal PET.

John A. Correia, *Member, IEEE*, Charles A. Burnham, *Senior Member IEEE*, David Kaufman, Anna-Liisa Brownell, and Alan J. Fischman

**Abstract**--We have completed construction of a second-generation, single-plane small animal PET instrument based on LSO detectors. The second-generation design addresses some of the limitations in the first-generation. The purpose of the work reported here was to characterize the physical performance of this instrument. Results of the performance measurements include: Spatial resolution = 1.25mm at field center and 1.5mm at 2 cm radius; point source sensitivity = 56 cps/uCi; scatter fractions of 0.019 and 0.056 in 3.8 and 6 cm diameter cylinders respectively; linearity of reconstructed signal within 5% up to 100 uCi/cc and acceptable dead-time performance up to 25k true cps. Examples of phantom and animal images are also presented.

## I. INTRODUCTION

During the recent past there has been a growing interest in the physiologic and biochemical imaging of small animals. Several factors have contributed to this interest. Firstly, the tremendous growth of the genetic engineering field has resulted in the development of a number of models of human disease in genetically manipulated mice and the study of such models is of great interest. Positron Emission Tomography (PET) provides the best available means of non-destructively studying the time course of general physiological parameters as well as specific biochemical changes in such disease models. Secondly, the pharmaceutical industry has become more and more aware of the advantages of non-destructive methods for preliminary drug kinetic studies. A major advantage of using PET for these studies is that the course of a labeled drug can be followed over time in a single animal thus requiring fewer animals and resulting in lower variability of parameter estimates due to tighter experimental controls.

The availability of new detector materials such as Lutetium Oxyorthosilicate (LSO), Yttrium Aluminum Pyrovanadate (YAP) and Gadolinium Silicate (GSO) for PET have led to the possibility of producing small-scale, high-resolution instruments which are appropriate for rodent imaging. The major properties of these materials that make higher resolution possible are high light output and fast light decay. Increased light output makes possible the identification of very small detectors while fast decay allows for fast timing and potentially high-count rate capability. There have recently

been a number of efforts toward the development of small-animal PET imaging devices. The earliest used Bismuth Germanate (BGO) detectors [1]. Cherry, et. al. [2][3] subsequently developed the first LSO-based animal-imaging instrument having approximately 2mm spatial resolution and volumetric imaging capability. A number of other investigators have developed scintillator-based systems at this resolution using either LSO [4][5], YAP [6][7] or GSO [8] scintillators and several different types of light readouts including position sensitive photomultiplier tubes and photodiode arrays [9][10]. Several investigators including ourselves have designed and constructed scintillator-based detector modules with resolution in the 1mm range [11]-[13]. Others have taken alternative approaches to the design of very high-resolution detector modules [14][15], for example stacked wire chambers with lead converter plates.

We have previously developed a single-plane, LSO-based-PET instrument with 1mm spatial resolution in objects on the scale of small animals [11]. Although this instrument performed well it was limited by low sensitivity due to the use of short crystals and by limitations in detector performance due to light losses at the center of the detector blocks. In order to address these issues, a second-generation instrument, Millimeter PET-II (MMP-II), which sacrifices a small amount of spatial resolution in order to improve detector performance was designed and constructed [16][17].

The purpose of the work reported here was to evaluate the physical performance of this recently completed second-generation instrument, which is intended to be a proof of concept for the LSO detector module design. Our eventual aim is to extend the design to a volumetric device.

## II. METHODS

### A. System Description

The second-generation system consists of a single 14.7cm diameter ring of 1.2mm wide by 7mm deep by 4.5mm high LSO crystals organized into 36 blocks of ten crystals each viewed by two photomultipliers. The blocks are positioned so that each block end is at the center of a photomultiplier. A total of 36 photomultipliers view the crystal array. The details of the light optics and surface preparations of the detector modules have been previously described [11][16]. Crystal events are identified via a series of block-specific look-up tables for crystal identification based on a normalized

difference in photomultiplier signals, energy bounds to account for variations in crystal response across blocks and gain corrections. These have also been described previously [11][16]. A diagram of the system electronics and data acquisition is shown in figure 1 and the instrument's design specifications are summarized in table 1.

Once a coincidence is identified all 36 photomultiplier signals are transferred through a buffered interface into a PC computer via the PCI bus. The crystal identification and binning computations are subsequently carried out in software. System singles rates are also transferred with each event for use in computing randoms and dead time corrections.

As demonstrated previously [16] modification of crystal-element size from 1x5x4.5mm to 1.2x7x4.5mm and improvement of light optics within the blocks leads to improved light collection compared to the first generation system (from 50-65%) and better identification of the end crystals.

### B. Performance Evaluation

In order to characterize the performance of the MMP-II system, a series of physical measurements have been carried out. These include measurements of spatial resolution, axial resolution, sensitivity, field uniformity, linearity and count-rate response. The measurement methods are described in detail below.

High contrast spatial resolution was measured using line sources of  $^{18}\text{F}$  placed axially in the field. Each source consisted of a 22ga stainless steel spinal needle (0.4mm i.d.) sealed with quick-drying epoxy after filling with approximately 30uCi of  $^{18}\text{F}$ . A series of data sets were collected for five minutes each with two sources in the field, one at the center and one at a radius which was varied in 0.5cm steps from collection to collection. The data sets were sensitivity corrected and reconstructed by filtered back-projection using a ramp filter and a zoom factor of two. FWHM and FWTM were measured from Gaussian fits to profiles through the source centers and corrected for finite source size.

The system sensitivity was measured for both a point source and an extended cylinder source of  $^{18}\text{F}$ . The point source consisted of 1.8 uCi of radioactivity absorbed into a cotton ball that been packed into the end of a 19gauge spinal needle. The cylindrical source consisted of a 4.5cm diameter by 4.5cm high plastic cylinder containing an initial radioactivity concentration of 8 uCi/cc. Sensitivity collections were carried out at low count rates such that the contribution to the total signal from random coincidences was below three percent and scattered coincidences are included in the sensitivity determination.

The energy bounds used were typical of those used in practice, approximately 60-125% of the crystal photopeak energies, and total counts were corrected for decay during acquisition.

The axial response of the instrument was measured using a collimator with a 4.5mm z-gap. This gap can be reduced to provide thinner slices by changing the collimator. Measurements were made at the field center and at 2cm

radius using a point source of  $^{18}\text{F}$  fabricated as described above. The source was stepped through the instrument in 0.1-mm increments. The total coincidence count rate was recorded at each point and all values were corrected for decay back to the start of the measurement sequence.

The uniformity of reconstructed signal was measured in a 4.5cm diameter cylinder filled with  $^{18}\text{F}$  solution. Data sets were collected for a series of four differing total counts, corrected for randoms, sensitivity variations and attenuation and by filtered back-projection reconstructed using a Hanning filter. A circular ROI encompassing the whole object was placed on each image and a histogram of the count distribution extracted. Since both statistical noise and non-uniformity contribute to the spreading of the histograms, an estimate of the non-uniformity contribution was made by extrapolating the measured standard deviation as a function of total events collected to infinite events.

The linearity of reconstructed radioactivity over a dynamic range of 10:1 was measured using an array of five 3mm-diameter cylindrical sources arranged in a radially symmetric pattern 1.5 cm from the center of a 4cm cylindrical plastic absorber. Image data sets were collected for 15 minutes duration at an interval of 2 hours. Data were corrected for attenuation, randoms and sensitivity variations and values of reconstructed signal were extracted from small regions-of-interest centered over the cylinders.

The system scatter fraction was measured for several cylindrical scatterer diameters. Polyethylene cylinders of 3.8cm and 6cm diameter were used as scattering medium. The former is close to the maximum object size that can be accommodated by the instrument and the latter represents more typical objects such as rodent torso. In each case a line source of  $^{18}\text{F}$  prepared as described above was placed at the center of the scatterer and a low count rate, moderate total count image was collected. The random rates for these collections were below 2%. The sources were aligned at the field center. Sinogram data were summed over angle to provide a single integrated projection. The scatter fraction was computed as the sum of all events in the region below 1% of the peak counts divided by the sum of all events.

The count-rate response of the system electronics was measured using a 3cm-diameter source of  $^{13}\text{N}$  in solution placed at the field center. A series of 2 minute data collections were carried out over a dynamic range of 500:1 in radioactivity concentration.

## III. RESULTS

The results of the measurements described in the previous section are presented in detail below and compared with simulated values where appropriate.

Figure 2. shows the results of the high contrast spatial resolution measurements. The measured FWHM resolution is 1.25mm at the center of the field and 1.5mm at 2cm radius. The FWTM, also illustrated, are consistent with a Gaussian response.

The measured sensitivities are presented in table 2 along with comparable values determined by Monte Carlo simulation. The point source sensitivity based on the

measurements described was determined to be 59 cps/uCi (0.16% of emitted photons) and that for the cylindrical source 386 cps/(uCi/cc). A separate set of measurements using a  $^{68}\text{Ge}$  point source gave comparable results.

The results of the axial response measurements are shown in figure 3. The axial resolution was measured from fitted Gaussians to be 1.9mm at the field center and 2.3mm at 2cm radius. Similar results were obtained in separate experiments using a  $^{68}\text{Ge}$  point source.

The results of the field uniformity measurements described above are shown in figure 4. The extrapolated non-uniformity at infinite count density resulting from this procedure is approximately 3.25%.

The system response to varying radioactivity concentration in 3mm diameter cylindrical objects is shown in figure 5. The measured concentrations and the corresponding linear least squares fit to them are consistent with linear response over a dynamic range of 10:1 in radioactivity concentration.

Figure 6 summarizes the scatter correction measurements described above. The integrated projection data for cylindrical scatterers of two different sizes is shown. The measured scatter fraction for the smaller (3.8cm diameter) cylinder was 0.019 and that for the larger (6cm diameter) was 0.056. The result for the smaller scatterer agrees well with the value of 0.025 predicted by Monte Carlo simulation but the measured result is somewhat higher than the Monte Carlo result of 0.04 for the larger.

Figure 7 shows plots of the singles, total coincidences, true coincidences and random coincidences over a 500:1 dynamic range of total coincidence count rate. The limiting useful count rate defined as that at which randoms equals trues was determined to be 29,000 true coincidences per second. At this rate the measured system dead time was 53%.

In order to demonstrate the system's imaging capability several extended objects were imaged. Figure 8 shows an image of a high-resolution Micro-Jaczcak phantom consisting of triangular arrays of cold rods surrounded by radioactivity. The rod diameters in mm are indicated and the rod spacing in each array is twice the rod diameter. The data were corrected for randoms, attenuation and non-uniformity but not scatter corrected. The data set collected consists of approximately 60 million events. The 1.5mm cold rods are well separated and a hint of the 1mm rods can be seen near the object center but they become blurred with increasing radius due to decreasing resolution.

Figure 9 shows the distribution of  $^{18}\text{F}$  radioactivity in the heart of a 25 gm mouse 45 minutes after the injection of approximately 2 mCi of FDG. The mouse is under anesthesia and no cardiac gating was used. The myocardial wall is clearly separated from the surrounding ventricle.

#### IV. DISCUSSION

A second-generation single-plane small animal PET has been completed and its properties evaluated experimentally. Most of the parameters evaluated agree reasonably well with those predicted in preliminary design studies. The measured sensitivities however are slightly lower than simulated values,

4% lower for the extended cylindrical source and 20% lower for the point source. These differences can be explained by the fact that additional events in the real system may be rejected based on energy criteria due to detector-block non-idealities. Similarly, the measured scatter fraction for the larger scatterer is higher than predicted by approximately 30%. This is as yet unexplained and may be the result of the data analysis method.

The system described here is a second-generation device intended to address some of the limitations of the first generation [11]. In the original system 5mm deep detectors were used in order to bias detection toward single interaction events. Subsequent simulation studies [17] showed that this depth could be increased to 7mm without a major increase in multiple interactions. Further the first-generation system was based on blocks of twelve 1mm wide crystals yielding 1mm spatial resolution at the center. This design yielded relatively high light losses at the center of the blocks and difficulties in identifying some end crystals. To address this limitation some resolution was sacrificed in the second-generation system to improve block performance. Crystal widths were increased to 1.2mm and organized in blocks of 10 resulting in a concomitant increase in detector-ring diameter from 12.5 to 14.6cm and a decrease in central resolution to 1.25mm. The overall effect of these changes was to increase sensitivity by approximately a factor of two and improve block performance considerably.

The intent of constructing the single-plane system described here was to develop approaches to detector design and data processing which could be extended to a volumetric system and such a design has been developed through bench-top studies and simulation [17]. However, a single-plane is still a useful tool for some types of small animal imaging studies, particularly those involving slowly varying radioactivity distributions such as  $^{18}\text{F}$ -FDG.

#### V. REFERENCES

- [1] Bloomfield PM, Rajeswaran S, Spinks TJ, et. al., "The design and physical characteristics of a small-Animal PET," *Phys. Med. Biol.*, vol 40, pp. 1105-1126, 1995.
- [2] Chatziioannou AF, Cherry SR, Shau Y, et. al. "Performance Evaluation of MicroPET: A high Resolution Lutetium Oxyorthosilicate PET Scanner for Animal Imaging," *J. Nucl. Med.* Vol. 40, pp. 1164-1175, 1994.
- [3] Cherry SR, Shao Y., Silverman R, et. al., "MicroPET: a high resolution PET scanner for imaging small animals," *IEEE Trans Nucl Sci* vol. 44, pp. 1161-1166, 1997.
- [4] Vaquero JJ, Seidel J, Siegel S, et. al., "Performance characteristics of a compact, position sensitive LSO module," *IEEE Trans Med Imaging*, vol. 17, pp. :967-978, 1998
- [5] Green MV, Seidel J, Vaquero JJ, et. al., "High Resolution PET, SPECT and Projection Imaging in Small Animals," *Comput. Med. Imaging Graph*, vol. 25, pp. 79-96, 2001.
- [11] Correia JA, Burnham CA, Kaufman D, Fischman AJ, "Development of a Small Animal PET Imaging Device with Resolution Approaching 1mm," *IEEE Trans. Nucl. Sci.*, Vol. 46, pp.631-635, 1999.

[12] Miyaoka RS, Kohlmyer SG, Lewellen TK, "Design of a micro crystal element (MICE) detector unit," *J. Nucl Med*, vol.41, p. 19P, 2000.

[13] Bevilaqua A, Bollini D, Del Guerra A, et.al., "A monte-carlo simulation of a small animal PET with 1mm resolution," *IEEE Trans Nucl Sci*, vol. 46, pp. 697-701, 1999.

[14] Bruyndoncks P, Liu X, Tavernier, et. al., "Performance study of a 3D small animal PET scanner based on BaF2 crystals and a photosensitive wire chamber," *Nucl Inst Meth*, Vol. A392, pp.407-413, 1997.

[15] Jeavons AP, Chandler RA, Dettmar CA, et.al., "A 3D HIDAC-PET Camera with Sum-millimeter Resolution for Imaging Small Animals," *IEEE Trans. Nucl. Sci.*, vol. 46, pp. 1067-1072, 1999.

[16] Correia JA, Burnham CA, Kaufman D, Fischman AJ, "Performance of a Small Animal PET Instrument with 1 mm Resolution," *IEEE Medical Imaging Conf, Conference Record.*, 1999.

[17] Correia JA, Burnham CA, Kaufman D, Fischman AJ, "Design Studies for volumetric high resolution small animal PET", *IEEE Medical Imaging Conf, Conference Record.*, 2000.

Figure 9:  $^{18}\text{F}$ -FDG image of a mouse heart in coronal section. The animal is anesthetized and no cardiac gating was applied. The myocardial wall and ventricle are well separated.

## Table and Figure Captions:

Table 1: Design Specifications of MMP-II Single-Plane Small-Animal PET.

Table 2: Comparison of measured and simulated sensitivities for point source and cylinder. Measurements were made with  $^{18}\text{F}$ .

Figure 1: Diagram of MMP-II Electronics and Data Acquisition.

Figure 2: Spatial resolution as a function of field radius measured with 0.4mm  $^{18}\text{F}$  line sources. Measurements are corrected for source size. FWHM and FWTM determined from Gaussian fits are shown.

Figure 3: Axial response measurements at field center and 2cm radius for 4.5cm z-gap. An  $^{18}\text{F}$  point source of 0.4mm diameter was stepped at 0.1mm steps axially through the field.

Figure 4: The standard deviation of the reconstructed pixel values over a 4.5cm cylinder of  $^{18}\text{F}$  at four levels of total counts.

Figure 5: Reconstructed values in 3mm cylinders located at 1.5cm radius in a 4cm absorber. Linear least squares fit to the measured values is also shown.

Figure 6: Measurement of scatter distribution from a line source of  $^{18}\text{F}$  at the center of two different sized tissue equivalent cylindrical absorbers. Shown is the sum of the projection data over all angles. The measured scatter fraction is 0.019 for the 3.8cm absorber and 0.056 for the 6cm absorber.

Figure 7: Count-rate performance: Shown are singles, total coincidences, trues and randoms measured with a decaying source of  $^{13}\text{N}$  solution contained in a 3.5 cm cylindrical container. The hundred-minute time scale corresponds to 10 half-lives or a dynamic range of approximately 500:1 in the data shown.

Figure 8: Image of a high-resolution Micro-Jaszczak cold spot phantom of diameter 4.5cm filled with  $^{18}\text{F}$ . The cold rod sizes in mm are indicated. The rod separation is two times the diameter in each array and the image contains 60M total coincidence events.

PARAMETER	MMP-II SPECIFICATION
Diameter (cm)	14.7
LSO Crystals	360
Element Size (mm)	.2 x 4.5 x 7
Number of PMTs	36
Resolution (mm) Center	1.2
Resolution (mm) 2.5 cm	1.8
Axial Resolution (mm)	1.7
Sensitivity (cps/uCi)	>70

SENSITIVITY	Measured	Simulated
Point (cps/uCi)	59	70
Point (percent)	0.16	0.19
4.5 cm Cylinder ( cps/uCi/cc)	386	402

